ELECTROTHERMAL PROPERTIES OF NANOWIRE MATERIALS FOR
ENERGY CONVERSION SYSTEMS

A DISSERTATION SUBMITTED TO THE DEPARTMENT OF MECHANICAL
ENGINEERING AND THE COMMITTEE ON GRADUATE STUDIES OF
STANFORD UNIVERSITY IN PARTIAL FULFILLMENT OF THE
REQUIREMENTS FOR THE DEGREE OF DOCTOR OF PHILOSOPHY

Saniya Akhtar LeBlanc

August 2012

This dissertation is online at: http://purl.stanford.edu/hv161nx0893

I certify that I have read this dissertation and that, in my opinion, it is fully adequate in scope and quality as a dissertation for the degree of Doctor of Philosophy.

Kenneth Goodson, Primary Adviser

I certify that I have read this dissertation and that, in my opinion, it is fully adequate in scope and quality as a dissertation for the degree of Doctor of Philosophy.

Christopher Edwards

I certify that I have read this dissertation and that, in my opinion, it is fully adequate in scope and quality as a dissertation for the degree of Doctor of Philosophy.

Alberto Salleo

Approved for the Stanford University Committee on Graduate Studies.

Patricia J. Gumport, Vice Provost Graduate Education

This signature page was generated electronically upon submission of this dissertation in electronic format. An original signed hard copy of the signature page is on file in University Archives.

ABSTRACT

Worldwide energy demand is projected to increase 40% by 2035. Thermoelectric power generators could be a rapid, powerful way to meet the increased need for energy by converting wasted heat energy into useful electrical energy. However, inter-disciplinary factors determining the feasibility of widespread thermoelectric power generation systems have been minimally explored. This work connects materials and manufacturing costs, materials properties, and system-level design to identify the factors necessary for successful thermoelectric generators.

Interest and investment in thermoelectrics for waste heat recovery and localized heating and cooling have flourished in recent years. The scalability and success of thermoelectric technology hinges on a combination of device efficiency and cost. The first part of this work develops cost-performance metrics for thermoelectric cooling and power generation using a device physics model, raw material prices, and estimated manufacturing costs. Both bulk and thin film materials and their respective manufacturing techniques are analyzed. The results indicate research and development targets that thermoelectric technologies must meet to be competitive in the marketplace.

Thermoelectric cogeneration offers an opportunity to recover waste heat from a variety of combustion systems. Computationally efficient simulations of practical systems that allow optimization and illustrate the impact of key material and system parameters are necessary. The second part of this work compares differences in thermoelectric material conversion efficiency and system-level power generation by simulating three combustion systems: a water heater, an automotive exhaust system, and an industrial furnace. A more detailed simulation for a 15 kW tankless, methane-fueled water heater further explores the potential for small-scale, stationary cogeneration. The simulation uses the finite volume method and links convective flow in a compact heat exchanger and conduction through the system to determine thermoelectric power generation. For a single water heater pipe, 126 W of electrical power can be generated, and a typical system could yield 370 W. While varying thermoelectric material parameters such as thermal conductivity can improve thermoelectric output by over 50%,

system components like thermal interface materials can severely limit power output. The impact of thermal interface resistance on power generation efficiency is established for all three combustion systems. The analysis demonstrates the impact system parameters have on the feasibility of thermoelectric waste heat recovery in combustion systems.

Engineering at the nanoscale produces materials with combinations of properties absent in the natural world, enabling tunable and enhanced energy conversion in these systems. In particular, zinc oxide nanowires may offer improved thermoelectric energy conversion. Heat generation along nanowires and near their electrical contacts influences the feasibility of energy conversion devices. The final part of this work presents ZnO nanowire electrical resistivity data and models electrothermal transport accounting for heat generation at metal-semiconductor contacts, axial thermal conduction, and substrate heat losses. The current-voltage relationships and electron microscopy indicate sample degradation is caused by the interplay of heat generation at contacts and within the nanowire volume. The model is used to interpret literature data for Si, GaN, and ZnO nanowires. This work assists with electrothermal nanowire measurements and highlights practical implications of utilizing solution-synthesized nanowires and realizing functional nanowire materials.

Finally, concluding remarks and perspectives on the future development of nanowires for energy conversion applications are provided.

ACKNOWLEDGMENTS

It has been a privilege and honor to work with the guidance of stellar Stanford University faculty members. Dr. Ken Goodson has served as my primary advisor. When I chose take a detour and strike out on a lesser known path by joining Teach For America before my Stanford graduate career, Ken demonstrated a level of support for which I will be forever grateful. He continued to provide this freedom of choice throughout my graduate career, even when granting that freedom delayed near-term gratification of predictable, tractable research progress. That freedom has allowed me to grow into a confident, technical leader. Whether it is at conferences, industry presentations, or academic and government meetings, Ken chooses to put his students at the forefront of the research when his own brilliance could easily dominate. In doing so, he has enabled me to develop technical proficiency and talent in ways that extend beyond traditional graduate research.

Dr. Alberto Salleo and Dr. Chris Edwards have served as invaluable advisors. Alberto's openness to research collaboration is evident in interactions with him and also in the terrific ethos of his group. His thoughtful guidance through our challenging experimental endeavors was essential. He indulged me many a time as I sought his input

during our shared commute to and from San Francisco. Chris contributed to my development throughout my Stanford career. He developed a challenging and influential course which fueled my enthusiasm for energy systems. I admire his thoughtful approach to teaching and education. Chris has also provided career mentoring over the years. The opportunity to openly discuss career options with an esteemed faculty member was much appreciated.

Many people have contributed to my research progress. In particular, I must thank two close collaborators. Dr. Sujay Phadke has become a valued colleague and friend. We bonded amidst hours toiling through nanowire experiment development, execution, and analysis – often in the dark both literally and figuratively. Shannon Yee's enthusiasm and broad-thinking has enabled an inter-university collaboration between the two of us that made the last year of my doctoral research particularly exciting and fulfilling.

My fellow group members of the Micro/NanoHeat Lab are talented individuals; I look forward to seeing their successful careers continue to unfold. Original senior students in the group Julie Steinbrenner, Roger Flynn, and Milnes David were great comrades and sources of support. Yuan Gao is a strong researcher whose quiet counsel I value. Shilpi Roy's genuine, down-to-earth friendship has kept me sane at times when I thought it was impossible. I cannot thank Joe Miler enough. He has been a friend, colleague, fellow philosopher, career counselor, and so much more; he has my utmost respect.

Much of my time has been spent engaging with wonderful people in the Stanford community and beyond. I am grateful to my Women in Science and Engineering group for providing sage counsel and support, particularly through my most trying experiences. My fellow American Society for Engineering Education leaders have been inspirational; I am proud of what we have created and accomplished together. I have had the good fortune of working with numerous K-12 and undergraduate students in communities in the Bay area and beyond. Their diversity, intention, and accomplishments energize me and renew my drive for educational equity. I must especially thank the strong women whose friendship and support have sustained me. I cherish my relationships with Polina Segalova, Ashley Kelley, Adela Bardos, Chelsey Simmons, and Rebecca Taylor more than words could express.

The unconditional support of my family has nurtured me. My LeBlanc family has welcomed me and continues to spoil me with love and attention. My aunt and uncle, Khala and Khalu, love me as one of their own, and I am endlessly grateful for the care they have shown. My two sisters, Salma and Sabrina, hold a special place in my heart. Without them, I would be lost and incomplete. My mother is my heart. By earning the first PhD in our family, I hope I have given her a gift she can cherish as much as I cherish her love and sacrifices. If this PhD has done nothing but make her proud, then it has done enough.

Each day I am fortunate to stand on the shoulders of giants to make my contributions to technology and society, and each day I am grateful to lay my head on the shoulder of my own giant, my husband. Travis believes deeply in my talent and potential. His brilliance and drive inspire me, and his support and love nourish me. I am thankful to have accomplished this endeavor with his partnership.

LIST OF TABLES

LIST OF ILLUSTRATIONS

NOMENCLATURE

A	heat transfer area
C_B	cost of material
$C_{M,B}$	manufacturing cost for processing based on volume
$C_{M,A}$	manufacturing cost for processing based on area
C_p	heat capacity
D	nanowire diameter
E	energy level
E_C	conduction band edge energy level
E_F	Fermi energy
F	electrode coverage factor
FF	fill factor
g	heat loss to substrate
G	cost-performance metric
h	convection coefficient
h_g	gas side convection coefficient
h_p	Planck's constant
h_w	water side convection coefficient
I	current
J	current density
k	thermal conductivity of TEM material
k_b	Bolztmann constant
k_e, k_p	electron and phonon contributions to thermal conductivity
k_s	substrate thermal conductivity
k_w	nanowire thermal conductivity
$K_{//}$	parallel thermal conductance in thermoelectric module
K_H	thermal conductance of system components on hot side
K_C	thermal conductance of system components on cold side
L	dominant length scale, leg length
L_m	electrode contact length

L_{opt} optimum leg length

L_s scattering length

L_T electrical transfer length

L_w nanowire length

$\dot{m}$ mass flow rate

m_{eff} effective mass of charge carrier

n carrier concentration

N doping concentration

P electrical power from TEM

q electron charge

q_g heat transfer rate from gas stream

q_h heat transfer rate from hot side

q_{Joule} Joule heating

$q_{Peltier}$ heat transfer due to Peltier effect

q_{TEM} heat transfer rate through TEM

q_w heat transfer rate to water stream

r nanowire radius

R electrical resistance

R_c thermal constriction resistance

R_f fluidic gap thermal resistance

R_L, R_{load} electrical resistance of load

R_m thermal contact resistance

R_{pw} thermal conduction resistance of pipe wall

$R, R_{TEM,e}$ electrical resistance of TEM

R_{th} thermal interface resistance

Ra_L Rayleigh number

S Seebeck coefficient

S_p, S_n Seebeck coefficients of p- and n-type legs

S_{pn} Seebeck coefficient of thermoelectric couple ($S_{pn} = S_p - S_n$)

$T_{g,i}$ gas inlet temperature

$T_{g,o}$ gas outlet temperature

T_o substrate temperature

T_p exterior pipe wall temperature

T_{pw} interior pipe wall temperature

t_{TEM} TEM thickness

$T_2, T_{TEM,c}$ TEM cold side temperature

$T_1, T_{TEM,h}$ TEM hot side temperature

T_w water temperature

U heat exchanger coefficient

VF radiation view factor

Z thermoelectric figure-of-merit

Greek symbols

ΔT_{lm} log mean temperature difference

ΔT_{TEM} temperature difference across TEM

ε heat exchanger effectiveness

ε_s semiconducting nanowire permittivity

η_o total fin surface efficiency

η_{TE} module thermoelectric conversion efficiency

η_{th} thermoelectric efficiency

η_{sys} system thermoelectric conversion efficiency

θ relative heat generation metric

Λ mean free path

Λ_{eff} effective mean free path

μ mobility

Π Peltier coefficient

ρ density

ρ_c electrical contact resistivity

ρ_w nanowire electrical resistivity

σ electrical conductivity

σ_{sb} Stefan-Boltzmann constant

σ_{TE} parasitic heat loss

TABLE OF CONTENTS

CHAPTER 1: INTRODUCTION

1.1 Overview of energy demand and use

Worldwide energy demand is projected to increase 40% by the year 2035 [1]. The use of every energy resource (oil, coal, gas, nuclear, hydro, biomass/waste, and other renewables) will increase. While the enthusiasm for renewable energy sources has grown, fossil fuels will continue to be the dominant resources used to feed energy demand. Hence, the near-term imperative is efficient use of these energy resources.
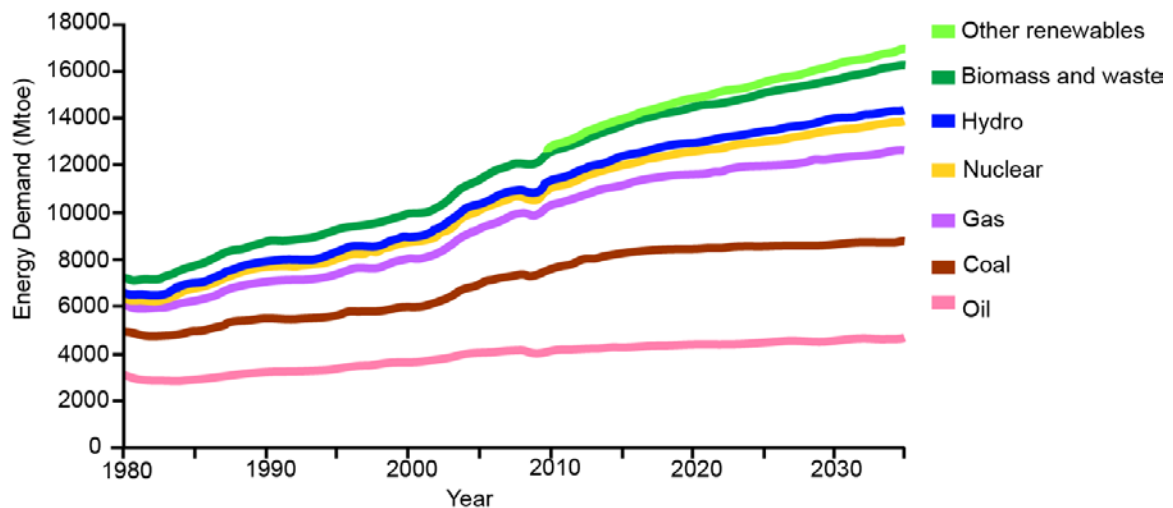
Figure 1.1: Worldwide energy demand history and projections broken down by energy resources used to supply the demand. Figure adapted from [1].

Energy use analyses convey an alarming reality. Less than fifty percent of the energy resources consumed are translated into energy services. The majority is rejected and not utilized [2]. For instance, vehicles are approximately 25% efficient. Combustion systems account for about 75% of energy used in manufacturing, but they are only 45% efficient [3]. There are two approaches to improving the use of energy resources. One approach is to improve the efficiency of the primary conversion processes themselves. Another approach is to convert the rejected energy into a useful form. Since rejected

energy primarily takes the form of thermal energy [2], conversion of heat into valuable energy services is paramount.
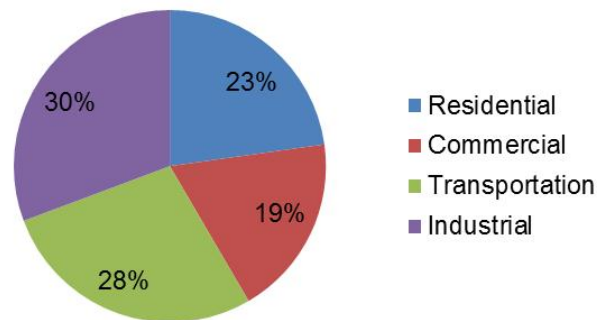
Figure 1.2: Energy use by sector in the U.S. Figure adapted from [4].

Energy use is projected to grow in all sectors (residential, commercial, industrial, and transportation). Electricity generation is increasing rapidly in these sectors, particularly as the electrification of the developing world escalates. While the combination of resources used to produce electricity will change, electricity demand will increase at an annual rate of 2.4%. In the U.S., electricity accounts for approximately 45% of residential and commercial energy use. Every energy resource will continue to be used for electricity generation.
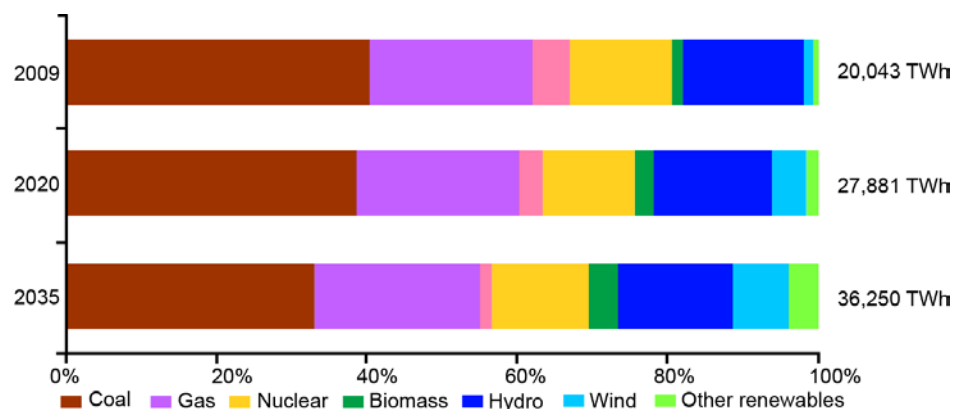
Figure 1.3: Breakdown of worldwide electricity generation by resource for 2009 and projections for 2020 and 2035. Figure adapted from [1].

Technologies which utilize rejected heat energy to generate electricity are thus timely and essential energy efficiency and electricity generation solutions. Stirling and Rankine cycles are often used to achieve this conversion of heat into electricity, but they involve an additional mechanical conversion step and require significant capital equipment investment. An alternative technology is thermoelectric generators, solid-state devices which convert heat directly into electricity. Thermoelectric generators have recently been proposed for waste heat recovery. Academic, government, and industrial research and development over the past decade point to a promising future for thermoelectric power generation.

1.2 Thermoelectric energy conversion

Thermoelectrics are solid-state devices which convert thermal energy to electrical energy. Operated in a reverse mode, thermoelectrics can use electricity to provide heating or cooling. Thermoelectrics provide localized control of energy transfer and distributed electricity generation. They have no moving parts and thus operate silently. To date, they have been reliable although new applications are challenging the reliability of current thermoelectric device technology. There are also considerable challenges associated with thermoelectric technology. The conversion efficiency is low, and performance is highly dependent on the device operating temperature, requiring specialized materials and devices for each application. System integration is particularly challenging as the devices require multiple materials with highly differentiated mechanical, thermal, and electrical properties.

The abundance of recent reviews on thermoelectrics from materials physics to applications demonstrates the newfound popularity of this technology [2, 5-9]. Thermoelectrics rely on the Seebeck effect which is illustrated in Figure 1.4 for a material in which electrons are the dominant charge carriers. When a temperature gradient is applied across a material, electrons with more energy on the hot side shift to the cold side. An electric field develops which prevents further electron flow. The Seebeck coefficient, or thermopower, is a measure of the voltage developed in response to the temperature drop across the material.
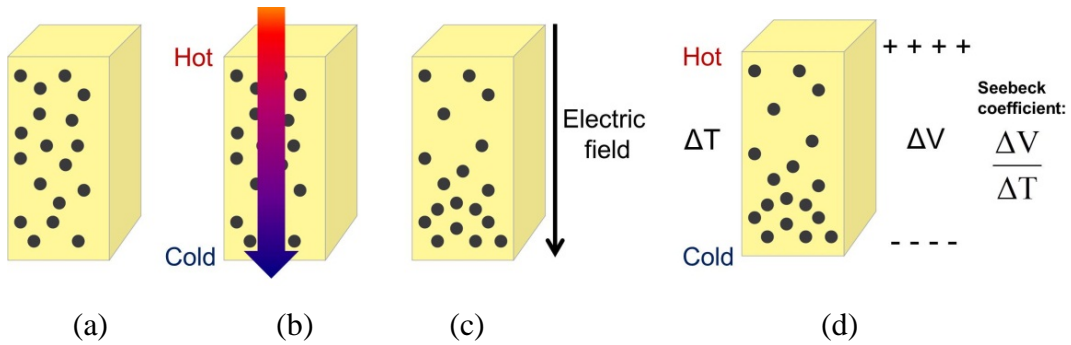
Figure 1.4: Depiction of the Seebeck effect in a material with electrons as the majority carriers. (a) Electrons are represented by the black dots and are evenly distributed in the material. (b) & (c) In the presence of a temperature gradient, a gradient in electron concentration results and gives rise to an opposing electric field. (d) The Seebeck coefficient represents the electric potential that results in response to the temperature gradient.
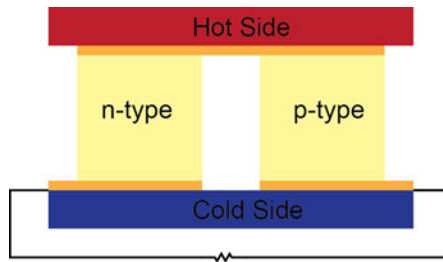
Figure 1.5: A typical thermoelectric module consists of n- and p-type semiconducting legs connected electrically in series through metal shunts.

A typical thermoelectric device depicted in Figure 1.5 has both n- and p-type materials where electrons and holes are the majority charge carriers, respectively. The semiconducting materials, or legs, are connected electrically in series with an electrical shunt, and multiple sets of leg couples can be connected to form a larger module. The leg couples are thermally in parallel. Two electrical insulating layers, typically ceramic plates, are on either side of the leg-shunt assemblies. In power generation mode, the module is connected to an external load resistance.

4

The thermoelectric figure-of-merit *ZT* is the commonly used metric by which thermoelectric materials are evaluated:

$$ZT = \frac{S^2 \sigma}{k} T$$

(1)

where *S, σ, k,* and *T* are the material Seebeck coefficient, electrical conductivity, thermal conductivity, and temperature, respectively. The numerator containing the power factor $S^2\sigma$ should be high while the denominator *k* should be low to achieve a high *ZT*. Detailed discussion of thermoelectric device physics and considerations will be presented in later chapters. The key point is as follows: a suitable thermoelectric material requires good charge transport while minimizing thermal energy carrier transport. However, there is an inherent conflict in achieving a high *ZT*. As shown in Figure 1.6, the Seebeck coefficient and electrical conductivity are inversely related, and the electrical and thermal conductivities are directly related.
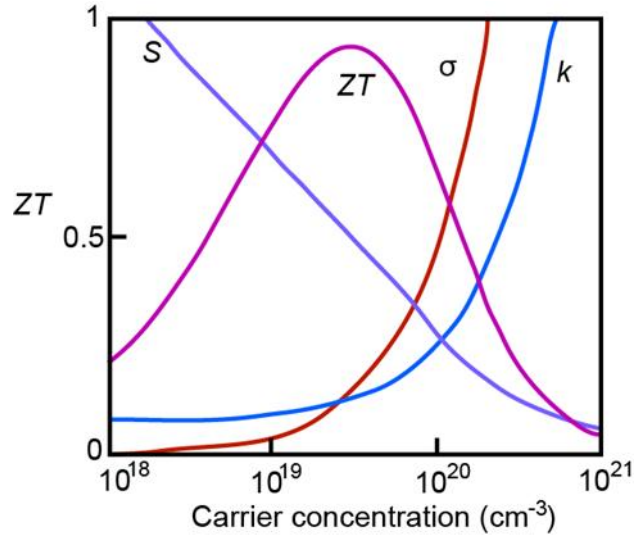
Figure 1.6: Variation of the properties composing *ZT* with carrier concentration. The tradeoffs between the properties result in a *ZT* function with a single maximum. Figure adapted from [5, 8].

This conflict is better understood by considering the property relationships developed through classical physics. A simplified Mott relation shows the Seebeck coefficient's inverse relationship with carrier concentration n [8]:

$$S = \frac{8\pi^2 k_B^2}{3qh_p} m_{eff} T \left(\frac{\pi}{3n} \right)^{2/3}$$

(2)

Conversely, the electrical conductivity is directly related to the carrier concentration:

$$\sigma = nq\mu$$

(3)

where the mobility μ also depends on carrier concentration. The thermal conductivity has two components from the electron and phonon, or lattice, contributions, k_e and k_p, to heat conduction such that $k = k_e + k_p$. The electron contribution to thermal conductivity is proportional to the electrical conductivity through the Wiedemann-Franz law:

$$k_e = L\sigma T$$

(4)

where the Lorenz number L is a proportionality constant. Hence, classical physics governing transport in traditional materials precludes tuning materials for ever higher ZT values.

Methods of enhancing ZT have been proposed. These methods rely on designing the materials chemistry and/or the use of low dimensional materials or low dimensional components within bulk materials [7, 10]. To increase the power factor, the electronic band structure must be altered to increase the Seebeck coefficient. Per the Mott equation, the Seebeck coefficient depends on the gradient of the density of states near the Fermi level E_F [6, 7]:

$$S = \frac{\pi^2 k_B^2 T}{3q} \left[\frac{1}{\sigma(E)} \frac{d\sigma}{dE} \right]_{E=E_F}$$

(5)

where E is the energy level. Semiconducting thermoelectric materials should be designed to have band gaps large enough such that doping leads to one type of carrier but narrow enough to achieve high doping and high mobility carriers. Such a material is termed a phonon glass-electron crystal material because the electrical and thermal properties are like crystalline and amorphous materials, respectively, all in a single material. Reducing a material's dimensionality alters the electron density of states and has been shown to increase the Seebeck coefficient without a significant reduction in electrical conductivity. Another method of increasing ZT is to reduce the phonon contribution to the thermal conductivity, k_p. The thermal conductivity is proportional to the mean free path Λ of the energy carriers. By introducing a scattering length L_s which is less than the dominant mean free path length, the effective mean free path Λ_{eff} can be decreased according to Matthiessen's rule [11]:

$$\Lambda_{eff} = \left[\frac{1}{\Lambda} + \frac{1}{L_s} \right]^{-1} \qquad\qquad (6)$$

The mean free path of phonons in a bulk material is on the order of hundreds of nanometers. Hence, the scattering length which is introduced must be in the nanometer to hundreds of nanometers length scale. The reduction in effective mean free path is accomplished through confinement from nanostructuring and/or interface scattering from boundaries, defects, and impurities. These methods of decreasing the effective mean free path, and thus the thermal conductivity, are depicted in Figure 1.7. In these ways, materials engineering and nanostructuring enable the engineering of material properties to achieve combinations of properties which do not naturally occur in materials. Several instances of nanostructured thermoelectrics with improved ZT values have been demonstrated through nanowire [12], nanostructured bulk [13], and superlattice [14] materials.
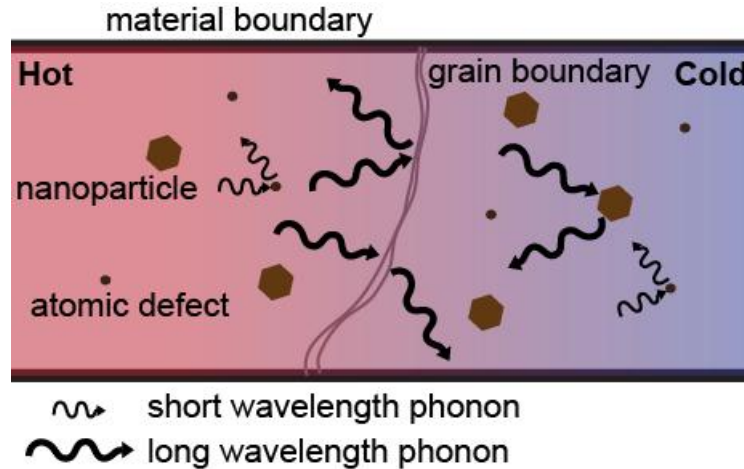
Figure 1.7 Schematic illustrating the ways phonons can be scattered in a material. Nanoparticles, grain boundaries, and the material's boundaries and surfaces scatter mid- and long wavelength phonons. Atomic defects scatter short wavelength phonons. Figure adapted from [15].

There are multiple classes of thermoelectric materials [6]. Traditional thermoelectrics have consisted of the chalcogenides bismuth telluride (Bi_2Te_3) and lead telluride (PbTe) as well as the binary semiconductor silicon germanium (SiGe). Newer complex inorganic structures such as clathrates, skutterudites, and half-Heusler compounds are in development. These often have atoms in interstitial sites of the crystal unit cell to act as phonon scattering centers, or rattlers. Oxide and silicide thermoelectrics have received some interest because of initial reports of favorable thermoelectric properties combined with source material abundance and affordability.

Existing applications of thermoelectrics are extremely limited. The primary application has been electricity generation onboard space exploration vehicles [16]. In this application, a radioisotope thermoelectric generator uses the heat from the radioactive decay of an isotope to power a thermoelectric [17]. Small thermoelectric modules are used for localized heating and cooling needs [18]. New applications in high temperature waste heat recovery using thermoelectrics have been proposed, particularly for automotive exhaust, industrial, and combustion appliance systems. Low temperature thermoelectric heat recovery options to supply small power requirements are less developed although they have been demonstrated for powering wireless sensors [19].

8

1.3 Outline of doctoral research

While the promise of thermoelectric power generation is exciting, there are many technical challenges to overcome in moving from their current limited use to the deployment of thermoelectric devices which impact energy supply and demand needs. The goal of this doctoral research has been to address these challenges by answering the following key question: *what factors determine the feasibility of thermoelectric power generation systems?*

The answers lie at the intersections between material properties, system design, and costs. The next three chapters detail these interactions. In the second chapter, a techno-economic analysis, sometimes referred to as a thermo-economic analysis, is applied to thermoelectrics. The analysis yields a thermoelectrics cost-performance metric which is used to evaluate state-of-the-art materials. The analysis and metric provide a tool to carry thermoelectrics research and development through the emerging technologies "valley of death" [20]. This work was accomplished in collaboration with Shannon Yee, Dr. Chris Dames, and Dr. Matt Scullin. The next chapter discusses a thermoelectric energy systems model which provides a tool for thermoelectric system development, demonstrates the difference between materials and system efficiency, and projects the impact of novel interface and thermoelectric materials. Partnerships with Bosch RTC supported this modeling. Finally, the role of enabling thermoelectric materials is explored using a specific study of a novel materials candidate, solution-synthesized zinc oxide nanowires. Electrothermal measurements and analysis of these nanowires demonstrate the significance of electrical contact resistivity on nanowire material characterization and product development. Collaboration with Drs. Sujay Phadke, Takashi Kodama and Alberto Salleo facilitated this work. Concluding thoughts and perspectives on the future of thermoelectrics and nanowire materials for energy conversion systems are provided in the last chapter.

CHAPTER 2: MATERIAL AND MANUFACTURING COST CONSIDERATIONS FOR THERMOELECTRICS

2.1 Introduction to thermoelectric thermo-economic analysis

Thermoelectrics are used in power generation and heating/cooling applications to convert heat to electricity and pump heat. To date, thermoelectrics have been constrained to niche applications such as space vehicle power sources. They have received renewed interest due to the development of higher performing materials and their potential to improve the efficiency of combustion systems through waste heat recovery [2, 7, 9]. Improvements in material performance are ongoing [6, 8, 21] since conversion efficiencies of typical thermoelectric materials are below 10% [5, 7].

Thermoelectric technology offers key advantages. With no moving parts, thermoelectrics are silent and reliable, and they allow localized control of energy transfer. Moreover, the physical form factor is flexible. Since multiple thermoelectric n- and p-type couples can be connected in series, a thermoelectric device can be smaller than a computer chip or larger than a solar panel. Nevertheless, considerable challenges associated with thermoelectric technology remain. Most notably, existing thermoelectrics have lower conversion efficiencies than alternatives such as organic Rankine cycles. Additionally, the reliability and durability of thermoelectric devices in a wide range of operating conditions have not been demonstrated. Challenges related to sublimation, oxidation, thermal and electrical interface degradation, and mismatched coefficients of thermal expansion are becoming increasingly critical for new thermoelectrics applications.

There have been technical and financial barriers to thermoelectric technology development. The cost of thermoelectric materials is prohibitive, largely due to the use of tellurium and germanium in traditional materials. Moreover, safety concerns will increasingly preclude toxic materials such as lead [22]. The weight and specific power of thermoelectric devices is particularly important for mobile applications such as vehicle waste heat recovery, yet few weight minimization solutions have been proposed. While government funding of thermoelectrics research and development has expanded

significantly in the past decade, the relative lack of familiarity with the technology made early-stage financing in the private sector comparatively slow to follow.

In spite of the remaining challenges, there are several indications the future of thermoelectric technology is bright. There has been a rapid development of higher performance materials due in part to nanostructuring and novel crystal structures [2, 6, 21]. Robust prototypes demonstrate the feasibility of thermoelectric devices for widespread, scalable applications [23-26]. Multiple start-up companies have received considerable recognition and funding while also forming strong partnerships with established academic and industrial research units [19, 27-30].

The development of scalable thermoelectric devices hinges on the both the device cost as well as energy conversion performance [2, 31]. Cost-performance analyses have been conducted for other energy technologies such as batteries and photovoltaics [32, 33]. This work develops cost-performance metrics for thermoelectric modules considering both conversion efficiency and materials and related processing costs. This enables an assessment of which materials may be most promising for specific applications and allows the present work to set performance targets for thermoelectric cooling and power generation applications. The costs of power generation (in \$/W) are reported by combining material properties reported for seven material classes, device physics, raw material costs, and estimates of manufacturing costs. The analysis is performed for five operating temperatures to reflect the myriad of potential thermoelectric applications. The difference in manufacturing costs for bulk versus thin film materials informs the feasibility of novel material use. A comparison to existing, competitive technologies highlights the targets thermoelectric technologies must reach both in cost and device performance to achieve success in the marketplace.

2.2 Development of a cost-performance metric
2.2.1 Device Physics

An appropriate cost metric for thermoelectric generation relates the electrical power output to the material and manufacturing cost of the generating module. A schematic of a thermoelectric module and an equivalent thermal circuit are depicted in Figure 2.1.

Detailed analyses of device heat transfer and power generation have been developed in earlier works [34-37].
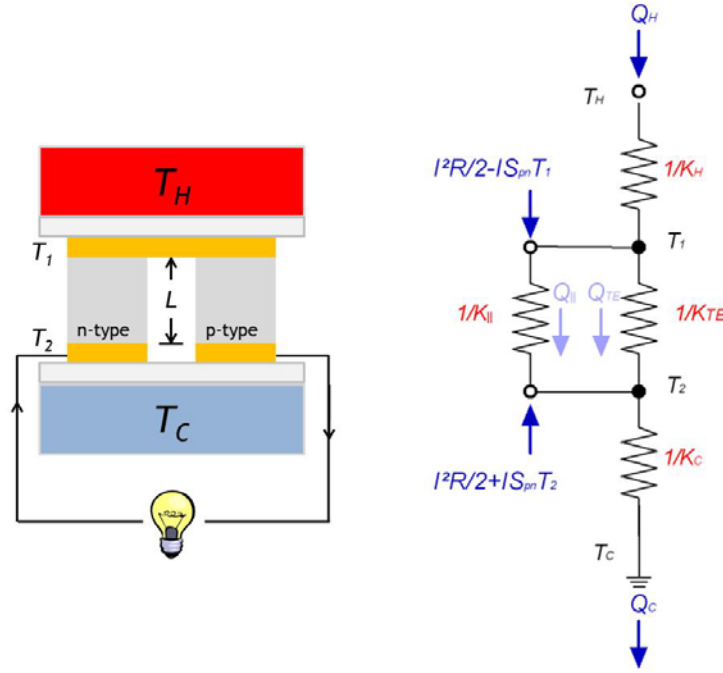
Figure 2.1: Schematic of thermoelectric module with an equivalent thermal circuit accounting for heat flow through the semiconducting legs as well as the air gap between the legs.

The electrical power output, P, of the module is the product of the heat flowing through the device, q_h, and the conversion efficiency of the device, η_{th}. Considering the two-legged module in Figure 2.1, an energy balance of the hot side at T_1 yields the heat flow through the device:

$$q_h = K_T \Delta T + S_{pn} I T_1 - \frac{1}{2} I^2 R \tag{1}$$

where K_T is the total thermal conductance of the module, $\Delta T = T_1 - T_2$ is temperature difference across the module, $S_{pn} = S_p - S_n$ is the thermopower difference of a pair of legs, I is the electrical current through the module, and R is the internal electrical resistance of

the module. The total thermal conductance is the sum of a parallel thermal leakage conductance, $K_{//}$, and the thermal conductance through the active material, K_{TE}.

For the device physics model, the following approximations are applied: (i) thermal and electrical contact/junction resistances are neglected, (ii) the cross sectional areas are constant along the length of each leg, (iii) material properties are evaluated at the average temperature between the hot and cold sides, (iv) the electrical resistance of the metallization layer is lumped with the electrical resistance of the thermoelectric material.

The thermoelectric generator efficiency depends on multiple material and module parameters and can take different forms. The electric power can be expressed as a function of current, I, or the open circuit voltage, V_{oc}, and the electrical resistance of the load, R_L, and of the module, R [34]:

$$P = I^2 R_L = \left(\frac{V_{oc}}{R_L + R} \right)^2 R_L = \left(\frac{S_{pn} \Delta T}{R_L + R} \right)^2 R_L \tag{2}$$

Combined with Equation 1 and the definition of efficiency, this yields

$$\eta_{th} = \frac{I^2 R_L}{K_T \Delta T + S_{pn} I T_1 - \frac{1}{2} I^2 R} \tag{3}$$

The figure-of-merit, $ZT = (S^2 \sigma / k) T$, simplifies the equation to

$$\eta_{th} = \left(1 - \frac{T_2}{T_1} \right) \left(\frac{m Z T_1}{Z T_m + m Z T_1 + (m+1)^2} \right) \tag{4}$$

where $T_m = (T_1 + T_2)/2$ is the average temperature, and $m = R_L/R$. Finally, optimizing m leads to the maximum idealized efficiency:

$$K_{\parallel} = 0, \; m_{opt} = \sqrt{1 + Z^*T_m} \Rightarrow \left(\eta_{th} \right)_{max} = \left(1 - \frac{T_2}{T_1} \right) \frac{\sqrt{1 + Z^*T_m} - 1}{\sqrt{1 + Z^*T_m} + \frac{T_2}{T_1}} \tag{5}$$

This is different from the efficiency at maximum power which occurs under load matching conditions (i.e., $R_L = R$ and $m = 1$):

$$m = 1 \Rightarrow \left(\eta_{th} \right)_{mp} = \left(1 - \frac{T_2}{T_1} \right) \left(\frac{ZT_1}{ZT_m + ZT_1 + 4} \right) \tag{6}$$

The efficiency at maximum power as expressed in Equation 6 is used to develop the cost-performance metrics described below.

The series thermal resistances ($1/K_H$ and $1/K_C$) are important for thermoelectric generator applications. Typical heat exchanger U-values were selected from literature based upon the application temperature and summarized in Table 2.4 [38, 39]. For thermoelectric cooling, the heat exchanger U-values were approximated in the limiting case of exchange between two low pressure (<1 bar) shell-and-tube heat exchangers. For low temperature recovery and solar thermal generation, the hot and cold side heat exchange were approximated as those from process water to a low pressure gas and from a low pressure gas to cooling water, respectively. For the high temperature applications (automotive exhaust or industrial process heat), the hot and cold side heat exchange were approximated as those from high pressure (150 bar) gas to low pressure gas and from a low pressure gas to cooling water, respectively. While the cost of the heat exchanger was not included in this analysis due to the large variability in cost based upon application, a reasonable value is $0.04/W [40].

The metallization layers and electrically insulating plates also add series thermal resistances. For the metallization layers, copper with a thermal conductivity of 400 W/m-K and a thickness of 25.4 µm was selected. For the heat spreading, electrically insulating top and bottom plates, alumina silicate with 30 W/m-K and a thickness of 0.38 mm was selected. The cost and of these materials was then approximated as $0.078/cm^2 based on catalogue pricing [41].

The parallel thermal conductance, $K_{//}$, has a significant effect on the module performance and must be accounted for correctly as it scales with the FF. In many applications, the volume between thermoelectric legs is likely to be occupied by a gas (*e.g.*, air). In these situations, the leg length will be such that conduction, convection, and radiation contribute.

For convection, the inside of the module can be treated as an enclosure where the Rayleigh number, Ra_L, a measure of the buoyant forces to viscous forces, is appropriate to determine the contribution of natural convection [39]. The critical length scale is the leg length. In most applications, dry air or possibly pure nitrogen will occupy that volume. Advection within the cavity occurs when $Ra_L>1708$. Otherwise conduction in the gas dominates. The convection coefficient is approximated with the relation:

$$\frac{\overline{h}L}{k} = 0.069 Ra_L^{1/3} Pr^{0.074} \qquad 3x10^5 \le Ra_L \le 7x10^9 \tag{7}$$

to yield the thermal conductance

$$K_{//,conv} = \frac{k_{air}(1-FF)A}{L}\left(0.069 Ra_L^{1/3} Pr^{0.074}\right)$$

$$= k_{air}\left(0.069\left(\frac{g\beta(T_h - T_c)}{v\alpha}\right)^{1/3} Pr^{0.074}\right)(1-FF)A \tag{8}$$

For low Ra_L, conduction through the gas dominates the parallel thermal leakage and can be expressed as:

$$K_{//,cond} = \frac{k_{air}(1-FF)A}{L} \tag{9}$$

For most leg lengths, conduction through the air gap will dominate. Even for large leg lengths, the resulting convection contributions are much smaller than those from conduction.

In addition to conduction and convection, radiation exchange may produce a non – negligible contribution. The configuration view factor and the surface emissivities dominate the radiation heat transfer between the hot and cold surfaces and are largely unknown across many thermoelectric applications. The configuration view factor for radiation exchange between two parallel plates is approximated as:

$$VF = \left(\sqrt{1 + \frac{L^2}{A}} - \frac{L}{\sqrt{A}} \right)^2$$

(10)

which is found from the 1D configuration view factor for two infinitely long, parallel plates of identical finite widths [39]. Thus, the radiation component of the parallel leakage is:

$$K_{//,rad} \approx \frac{\sigma_{sb} T_m^3 \left(1 - FF \right) A}{\left(\frac{\left(1 - \varepsilon_1 \right)}{\varepsilon_1} + \frac{\left(1 - \varepsilon_2 \right)}{\varepsilon_2} + \frac{1}{VF} \right)} \approx \frac{\sigma_{sb} T_m^3 \left(1 - FF \right) A}{\left(1 + \frac{1}{VF} \right)}$$

(11)

where σ_{sb} is the Stefan-Boltzmann constant, and ε_i is the emissivity of the parallel plates which is assumed to be $\varepsilon = 2/3$ for both plates. Figure 2.2 shows convection/conduction through the air gap dominates the total parallel thermal leakage. The radiation component is non-negligible even at low temperatures (*e.g.*, T_m=60℃) and becomes more significant at higher temperatures.
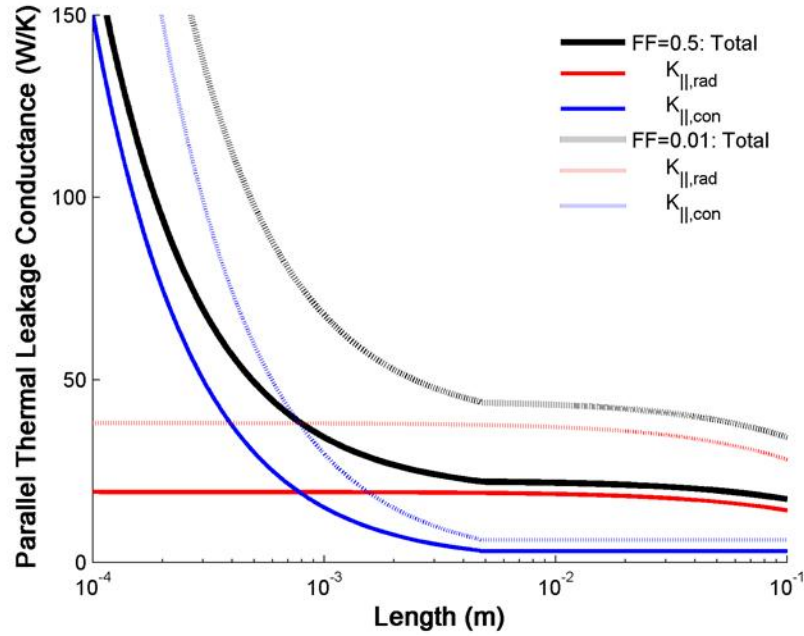
Figure 2.2: Parallel thermal leakage conductance vs. length for T_m=60℃. The parallel thermal conductance for all fill factors (dashed vs. solid lines) is dominated by the conduction (blue lines) through the air gap which increases as the legs become shorter. The radiation contribution (red lines) becomes more significant at higher temperatures but is non-negligible even at lower temperatures; it is not the dominant contribution except for large leg lengths.

2.2.2 Cost-Performance Metric

Both material cost and manufacturing costs are utilized to develop a cost-performance metric. The costs are determined based on a conceptual estimating technique [42] since these devices are largely unprecedented. Rapid iterations on cost estimates completed in tandem with thermoelectric product development will prove valuable as devices enter the market.

The cost of the extracted raw material C_B captures the fundamental differences in material costs. The material cost is determined from the 2011 price of each element as reported by the U.S. Geological Survey. It is based on the worldwide production of the element and represents the average price an industrial consumer would pay [43]. Thermoelectric materials are typically composed of raw materials which have been

processed to a purity level of 99% or higher. Typical costs for pure materials are presented in the supplement information and can be significantly higher than the raw material cost. For instance, aluminum is an abundant material with a raw material cost of $2.60/kg. However, the cost of 99.999% pure aluminum is approximately $300/kg [44]. While purification adds to the material cost [45], the cost of purified materials is highly uncertain. It can vary significantly by vendor and is strongly influenced by rapidly changing market and processing factors [46-49]. This volatility can convolute the cost-performance analysis, so it is omitted here. This approach does not bias the results for particular materials since the purification conditions apply to many minerals [33]. Table 2.1 provides a comparison of the raw material cost [50] to the cost of purified powders [48]. The cost of purification will be a consideration for the development of thermoelectric devices, and decisions regarding in-house purification or purchasing purified stock will be required, particularly as production volume increases.

Table 2.1: Raw and purified thermoelectric material costs for a selection of the materials analyzed in this work.

Material Name	Raw Material Cost ($/kg)	Pure Material Cost ($/kg)
Bi_2Te_3	110	1100
PbTe	81	700
SiGe	678	9400
Si	3	240
$Ba_8Ga_{16}Ge_{30}$	644	9500
$Yb_{0.2}In_{0.2}Co_4Sb_{12}$	24	270
$(Zn_{0.98}Al_{0.02})O$	2	67

Manufacturing costs are divided into two categories based on the method of material processing. Processes enacted on the entire volume of material such as ball milling and spark plasma sintering have costs denoted by $C_{M,B}$. Other processes like dicing and metallization depend on the area of material processed; these costs are indicated by $C_{M,A}$. The required throughput of thermoelectric material in a manufacturing process will depend on both the performance of the material and the yield of the process. Fewer legs will be required for higher performing materials, and less material must be processed as yield improves. Throughput is highly dependent on the specific application and product,

18

so it is not easily generalizable to a broad analysis. To make this analysis broadly applicable, an activity measure [42] has been assigned to the manufacturing equipment considered here which assumes the equipment will be in operation year-round. Manufacturing equipment costs are approximate and estimated for new equipment. Equipment is typically tailored specifically for the end-use application, so communication with vendors is required for accurate quotes and precise costs. Particularly in early stage research, development, and production, tools built in-house or used/refurbished equipment may be used to reduce costs. In some cases, it may be more cost effective to use a service provider or user facility for certain manufacturing steps rather than purchasing equipment and performing the process in-house [51-53]. This is a common practice for early-stage development requiring semiconductor processing techniques.

The manufacturing costs are summarized in Table 2.2. Figure 2.3 depicts the cost for processing bulk and nano-/micro-structured materials as well as the module and heat exchanger costs required for all devices. They are classified by processes which are done on bulk and film materials. Some processes performed on bulk materials depend on the amount of material processed. The remaining processes depend on the amount of area processed. The cost is calculated by dividing the equipment cost by the equipment lifetime and throughput. In most cases, the cost and throughput of equipment was obtained from quotes or estimates provided by equipment vendors. A 20 year equipment lifetime and 24 hour per day, 365 days per year operation were assumed. Additional costs of tooling, maintenance, repair, assembly (automated or manual), overhead, and labor are not included in this analysis.

The metallization cost denotes the deposition of diffusion barriers and metallization to improve contact to the electrical shunt. It includes both the cost of the equipment and an approximate cost of the metal deposited. An additional $90/m^2$ was added to represent the metal cost. This was determined by estimating the cost of sputtering 1 µm of metal with >99% pure metal targets at $10,000/kg with a density of 9000 kg/m^3 [48].

The cost of performing molecular beam epitaxy depends on the amount of material deposited since the throughput is highly dependent on deposition layer thickness. A

typical deposition rate of 1 µm/h was assumed with an equipment cost of \$11.42/h. The density of PbTe was used to approximate the manufacturing cost in \$/kg.

Table 2.2: Manufacturing costs for processes required to make thermoelectric modules.

	Process	Cost ($/kg, bulk) ($/m², area)	Equipment cost ($)	Equipment throughput (kg/day, bulk) (m²/day, areal)	Ref.
Bulk processing	Ball milling	1.10	40,000	5	[54]
	Melt spinning	0.77	135,000	24	[55]
	Spark plasma sintering	1.30	385,000	42	[56]
Area processing	Dicing	47	150000	0.44	[57]
	Metalization	120	200,000	0.88	[46, 49, 58]
	Low-level microfabrication	150			[59]
	Medium-level microfabrication	2500			[59]
	High-level microfabrication	10,000			[60]
	Screen printing	4.80	50,000	1.4	[61, 62]
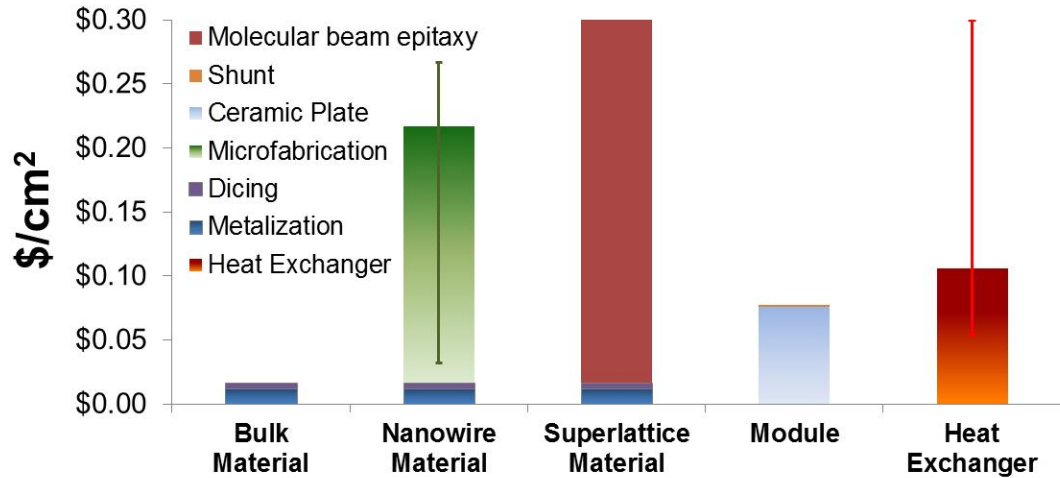
Figure 2.3: Manufacturing, module, and heat exchanger costs for thermoelectric devices made of bulk, nanowire, and superlattice materials. The range bars for nanowire materials correspond to the intensity of microfabrication processes, namely the number of fabrication steps. The heat exchanger costs correspond to values for newly developed heat exchangers and off-the-shelf exchangers of varying effectiveness [41, 63].

The analysis presented here is not a comprehensive cost estimate designed to replace a cost estimation performed by management to determine pricing. Rather, this work specifically addresses the cost of candidate materials and the cost to process those materials into thermoelectric legs for a module. It enables realistic assessments of current and future materials' potential for use in cooling and power generation applications by linking technical performance with estimated material and equipment costs.

The material and manufacturing costs described above can be evaluated on an area basis in $/m^2 as:

$$\left(C_B + C_{M,B}\right)\rho L + C_{M,A} \tag{12}$$

where ρ is the density, L is the thickness, C_B is the cost of the raw material, $C_{M,B}$ is the manufacturing cost associated with the material, and $C_{M,A}$ is the manufacturing cost for area-based processes.

Using the area of the device, A, the cost to produce a watt of electricity is expressed as the primary metric for power generation G in $/W:

$$G = \frac{\left[\left(\left(C_B + C_{M,B}\right)\rho L + C_{M,A}\right)\right]AFF}{\eta_{TE}q_h} \tag{13}$$

where FF represents the fill factor which is a ratio of the area of the active material to the total area of the module. This metric relies heavily on the device physics embodied by η_{TE} and q_h. The optimum leg length, L_{opt}, is determined by numerically minimizing the metric G. As shown in Figure 2.4, the optimum leg length derived from a cost minimization procedure is not the same as the leg length determined from merely considering maximum efficiency or power output.
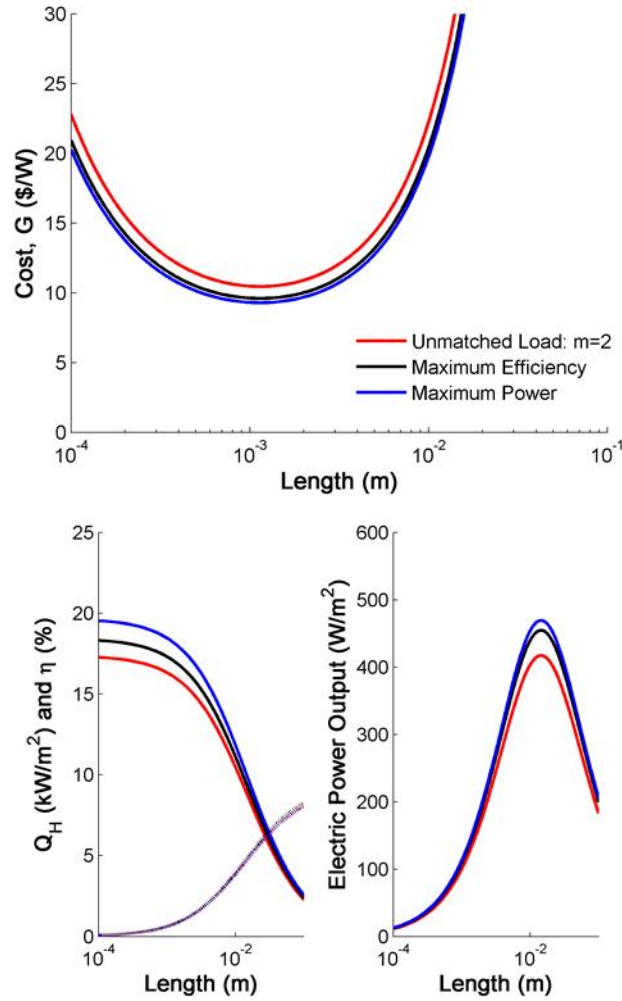
Figure 2.4: Example L_{opt} and cost minimization for material bulk $Bi_{0.52}Sb_{1.48}Te_3$ with $T_m=135℃$, $A=1$ m^2, and $F=1$. The leg length that gives the minimum cost is not the same length that maximized the efficiency or output power.

2.2.3 Analysis Parameters

As summarized in Table 3, state-of-the-art materials used in the analysis are from the main classifications: chalcogenides, silicides, clathrates, half-Heuslers, skutterudites, and oxides. A novel polymer material, PEDOT:PSS, has recently been proposed for thermoelectrics and is also included here [64]. Both bulk and film materials are considered with the latter referring to thin film, superlattice, and nanowire materials. The material properties were taken from the characterization results reported in the references listed in Table 2.3. Materials are also designated by the presence of nanostructuring.

Nanobulk materials are ones which were identified by the original authors as having nanoscale grain structures.

Potential thermoelectric power generation applications span a large range of operating temperatures. Therefore, the cost-performance analysis of the materials in Table 2.3 was conducted for five operating temperatures representing various proposed applications as shown in Table 2.4. Since the fill factor is a significant consideration for both cost and performance, five fill factors were analyzed.

The material properties were taken from results reported in the cited references. In some cases, the materials were not characterized over a temperature range which included the temperatures T_m analyzed here. When the minimum/maximum temperature reported was within fifty degrees of the temperatures analyzed, linear extrapolation using the first/last two data points was implemented to obtain a predicted material property at the target temperature. Otherwise, the analysis excluded the material in the temperature ranges where properties were unavailable.

Table 2.3: Material Identification Table. Color coding identifies material types as follows: red for chalcogenides, LAST and SiGe, blue for silicides, purple for clathrates, green for skutterudites, black for oxides, yellow for half -Heuslers, grey for polymers.

ID #	Material Name	Material Class	Material Cost ($/kg)	$T_m = 60$ C, $FF = 0.5$		Ref.
				L_{opt} (mm)	ZT_m material	
1	Bi_2Te_3	Bulk	110	0.51	0.74	[65],[53]
2	$Bi_{0.52}Sb_{1.48}Te_3$	Bulk	125	0.51	1.05	[66]
3	$Bi_{0.52}Sb_{1.48}Te_3$	Nanobulk	125	0.50	1.52	[66]
4	$Bi_{0.54}Te_{0.46}$	Nanowire	84	0.39	0.02	[67]
5	$(Na_{0.0283}Pb_{0.945}Te_{0.9733})(Ag_{1.11}Te_{0.555})$	Nanobulk	81	0.50	0.19	[68]
6	Bi-doped $PbSe_{0.98}Te_{0.02}$	Superlattice	55	0.05	1.96	[69]
7	$AgPb_{18}SbTe_{20}$	Bulk	84	0.53	0.01	[70]
8	SiGe	Bulk	678	0.50	0.09	[71]
9	$Si_{80}Ge_{20}$	Nanobulk	371	0.50	0.16	[71]
10	SiGe	Nanowire	679	0.80	0.22	[72]
11	$Mg_2Si_{0.85}Bi_{0.15}$	Nanobulk	7	2.45	0.09	[73]

12	$Mg_2Si_{0.6}Sn_{0.4}$	Bulk	4	2.20	0.20	[74]
13	Si	Nanobulk	3	4.77	0.03	[75]
14	Si	Nanowire	3	0.80	0.72	[76]
15	$MnSi_{1.75}$	Bulk	2	1.75	0.05	[77]
16	$Mn_{15}Si_{28}$	Nanobulk	2	1.92	0.07	[77]
17	$Ba_8Ga_{16}Ge_{28}Zn_2$	Bulk	615	0.50	0.12	[78]
18	$Ba_8Ga_{16}Ge_{30}$	Bulk	644	0.50	0.06	[79]
19	$Ba_7Sr_1Al_{16}Si_{30}$	Bulk	2	0.52	0.02	[80]
20	$CeFe_4Sb_{12}$	Bulk	37	0.50	0.20	[81]
21	$Yb_{0.2}In_{0.2}Co_4Sb_{12}$	Bulk	24	1.31	0.32	[82]
22	$Ca_{0.18}Co_{3.97}Ni_{0.03}Sb_{12.40}$	Bulk	13	2.26	0.20	[83]
23	$(Zn_{0.98}Al_{0.02})O$	Bulk	2	9.53	0.01	[84]
24	$Ca_{2.4}Bi_{0.3}Na_{0.3}Co_4O_9$	Bulk	30	0.87	0.03	[85]
25	InGaZnO	Nanowire	511	0.80	0.07	[86]
26	$Na_{0.7}CoO_{2-\delta}$	Bulk	36	2.71	0.04	[87]
27	$Zr_{0.25}Hf_{0.25}Ti_{0.5}NiSn_{0.994}Sb_{0.006}$	Bulk	10	0.70	0.49	[88]
28	$Zr_{0.5}Hf_{0.5}Ni_{0.8}Pd_{0.2}Sn_{0.99}Sb_{0.01}$	Bulk	9	0.50	0.18	[89]
29	$Ti_{0.8}Hf_{0.2}NiSn$	Bulk	11	0.82	0.04	[90]
30	PEDOT:PSS	Polymer	0.34	1.50	0.01	[64]

Table 2.4: Device temperatures and example applications. Fill factors of 0.001, 0.01, 0.1, 0.5, and 1 were analyzed.

Applications	Low temperature recovery	Solar thermal generator	Automotive exhaust heat recovery	Industrial furnace heat recovery
Hot side, T_h (°C)	100	250	500	800
Cold side, T_c (°C)	20	20	50	50
Average, T_m (°C)	60	135	275	425
Hot side U-value, U_h (W/m^2-K)	102	102	120	120
Cold side U-value, U_c (W/m^2-K)	105	105	105	105

Unless the material density was reported with the measured material properties, the theoretical density was used. Multiple manufacturing processes result in thermoelectric

materials whose density is less than the theoretical density. For instance, most techniques involving pressing stoichiometric compositions of powders create thermoelectric material pellets which have microscopic air pockets causing the pellet density to be approximately 80% of the theoretical value.[77] One key exception is the spark plasma sintering technique which produces pellets >90% relative density.[91] The density of nanowire materials is also different than the theoretical density. Each leg of nanowire material has a density which depends on the nanowire fill factor and the density of a matrix material around the nanowires. This analysis approximates the thermoelectric leg density as the nanowire material's density which is likely an overestimate of the density. Since the power density scales with the nanowire and module fill factors, the module fill factor can be adjusted based on the nanowire fill factor, so this estimation does not change the outcomes of the analysis.

It is difficult to characterize thermoelectric properties of thin film materials [14, 69, 92]. Through-plane thermal conductivity and Seebeck coefficient are often reported with in-plane electrical conductivity. To determine the thermoelectric performance of superlattice materials, the Harman method has been used to measure ZT directly. The analysis here is conducted with a superlattice where the Seebeck coefficient was measured. Electrical resistivity was calculated from reported carrier concentration n and mobility μ using $\sigma = nq\mu$ with the electron charge q. The thermal conductivity was extracted from the measured data.

2.3 Cost-performance of thermoelectric materials and applications

The cost performance analysis yields results which indicate the cost competitiveness of thermoelectric technologies for cooling and power generation. The cost performance analysis for thermoelectric power generators demonstrates the cost competitiveness of this technology as well as perspective on future materials development. Figure 2.5 shows the cost of thermoelectric devices for each of the operating temperatures considered. The strong dependence of cost on fill factor is expected since a larger fill factor indicates use of more material. Even for a given fill factor, the costs for devices made out of different materials can vary by one to three orders of magnitude. Since material properties are temperature-dependent, these results indicate which materials could not be considered for

certain applications, particularly when alternative technologies are more affordable. This is particularly relevant for applications operating near the lowest temperature, $T_m = 60°C$, considered since there is a dearth of thermoelectric materials with high performance at low temperatures, so the costs are predominately above \$1/W. For each application, it is pertinent to compare these thermoelectrics costs to the cost of other electricity generation technologies. For instance, the current cost of photovoltaics is \$1/W, and the photovoltaic cost is project to quickly reach \$0.50/W [93]. Particularly for high temperature waste heat recovery, a competitive technology is the organic Rankine system. The cost for such systems is approximately \$4-5/W [94].

In Figure 2.6, the materials are plotted for two parameters of interest: the total costs as represented in Equation (9) and the figure-of-merit ZT_m. The reference bars are drawn for a reference chalcogenide material. These plots provide an image of the current materials landscape and inform future materials research. There is a paucity of materials in the lower right-hand quadrant indicating materials which are less expensive and higher performing than the chalcogenide references. The clustering of points below the standard material's cost point indicates significant research and development work lies in developing higher performing materials which are not more expensive to produce than the standard bulk materials. For instance, nanowire materials requiring microfabrication processes are not currently competitive options.

26

(b)
$T_m = 135°C$

(c)
$T_m = 275°C$

(d)
$T_m = 425\,°C$
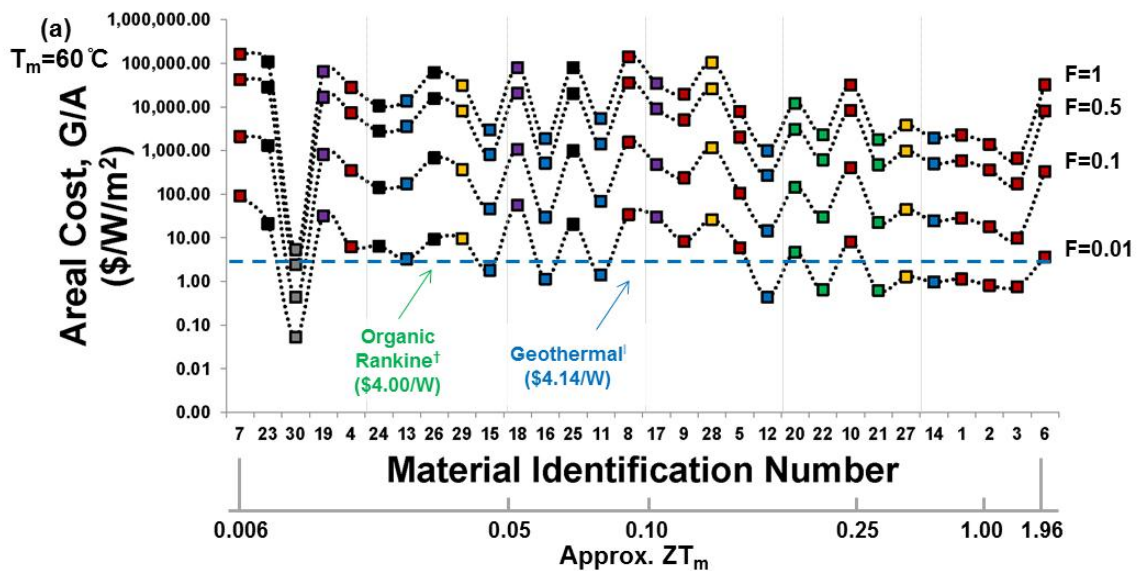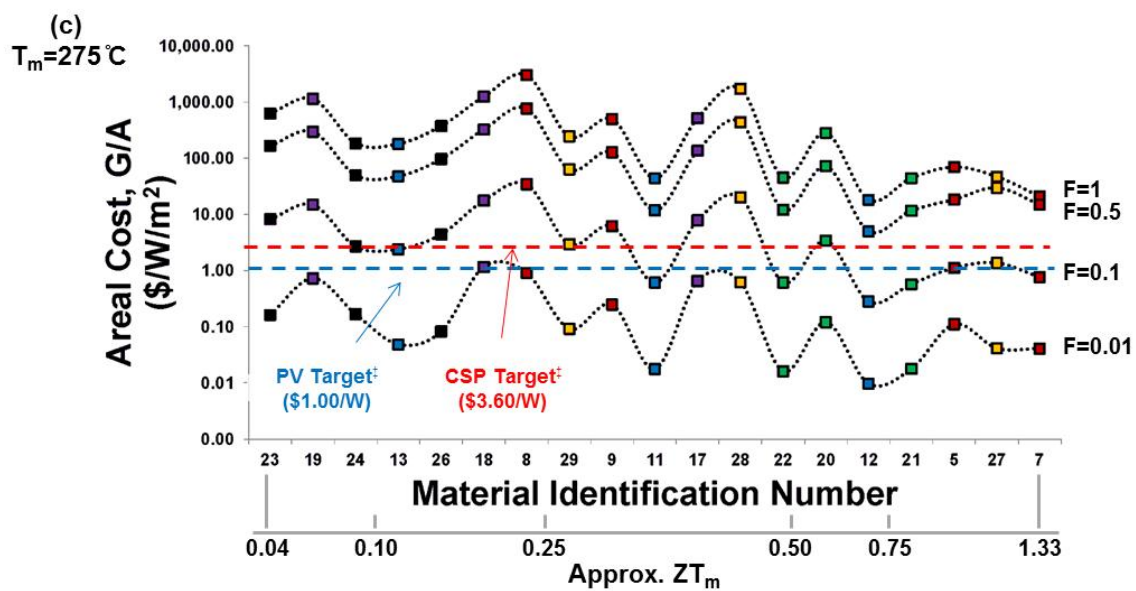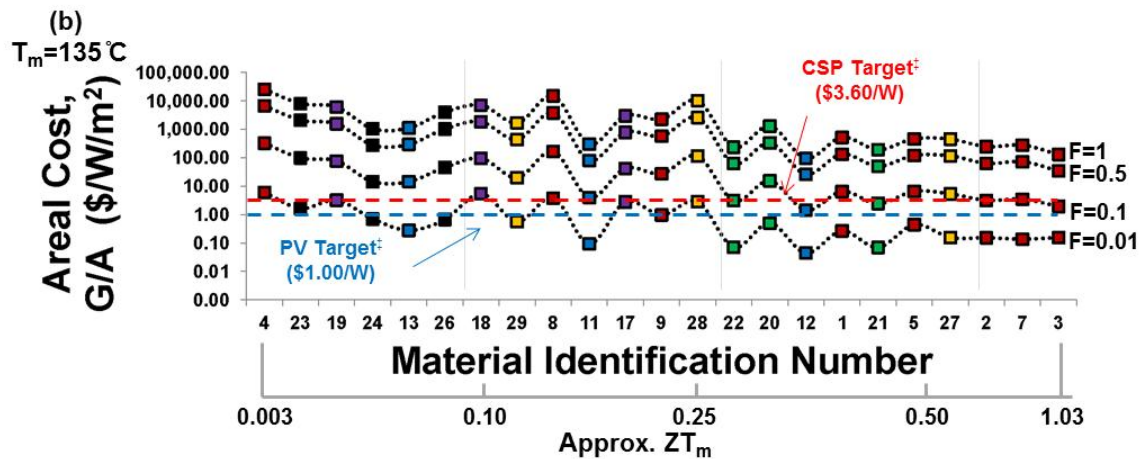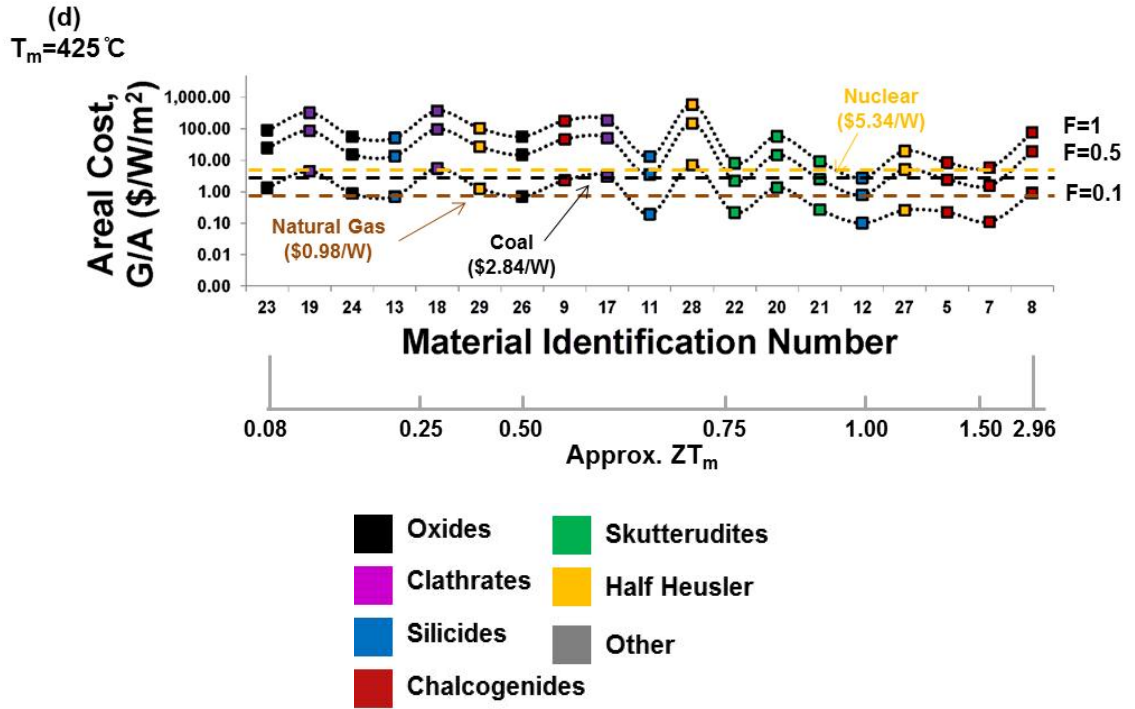
Figure 2.5: Select $/W cost comparison charts: (a) $T_m = 60\,°C$ applications, (b) $T_m = 135\,°C$ applications, (c) $T_m = 275\,°C$ applications, and (d) $T_m = 425\,°C$ applications. Horizontal lines represent application competition targets.
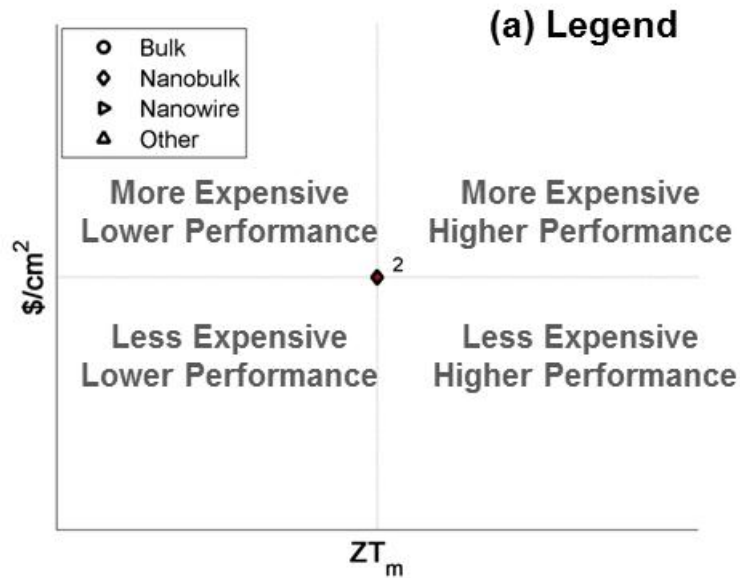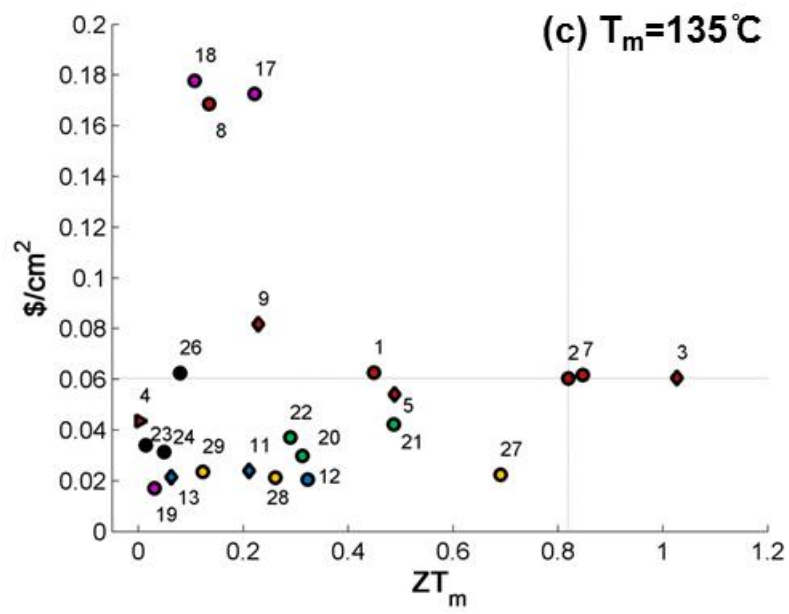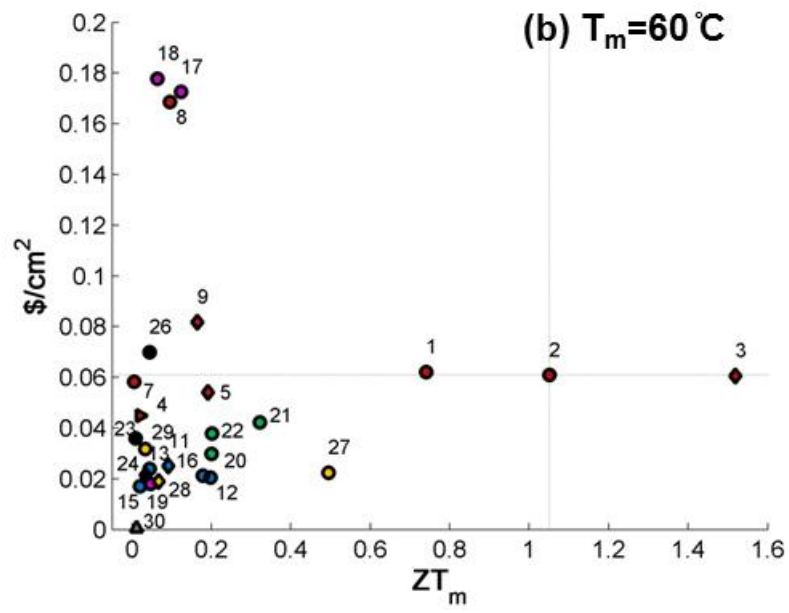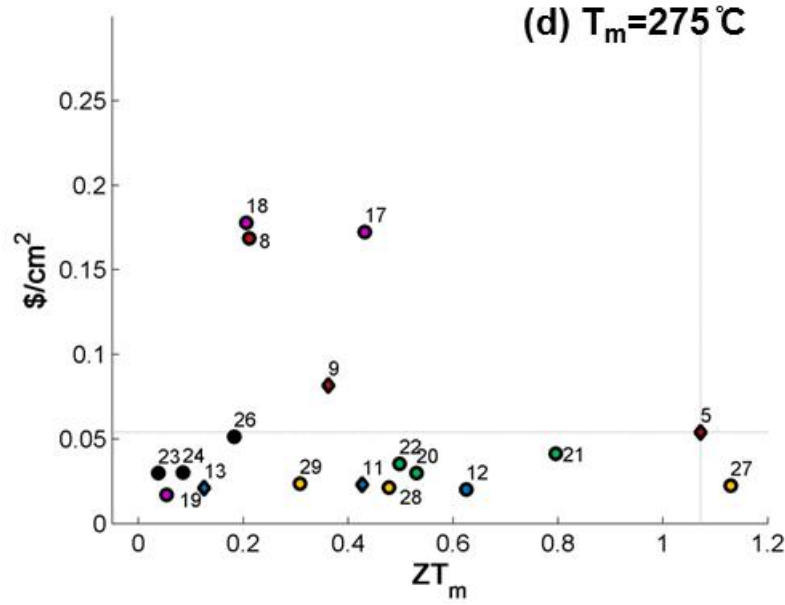
(b) $T_m=60\,^{\circ}\mathrm{C}$

(c) $T_m=135\,^{\circ}\mathrm{C}$

Figure 2.6: Areal cost vs. ZT_m scatter plots: (a) legend, (b) $T_m = 60\,°C$ application, (c) $T_m = 135\,°C$ application, and (d) $T_m = 275\,°C$ application. The horizontal and vertical lines represent comparisons to material 2 for low temperature and 5 for high temperature applications. The shapes represent the material class: bulk, nanobulk, nanowire, other.

This work provides a first-of-kind thermoelectrics cost-performance metric which incorporates material properties, device physics, raw material costs, and manufacturing costs. The analysis and resulting cost-performance values provide a tool for thermoelectric device research and development at the laboratory and commercial levels. A key aspect of the work includes thermoelectric leg geometry optimization through the minimization of the cost combined with performance rather than optimization of efficiency or power generation alone. The results demonstrate the status of current state-of-the-art thermoelectric materials relative to competitive power generation technologies for a range of application temperatures. Devices with low fill factors can be cost-competitive if the overall power generated is deemed sufficient. Although novel nanowire and superlattice materials reported to date are touted as promising, they appear uncompetitive for near-term applications due to low performance and the significant costs associated with microfabrication manufacturing techniques. Even considering the use of affordable materials, considerable performance gains must still be achieved for

these materials to be competitive. When applied to several traditional and new thermoelectric material classes, the analysis demonstrates the paucity of materials which are both higher performing and lower cost than standard chalcogenides. The realization of commercial thermoelectric devices hinges on the simultaneous improvement and optimization of material properties, system design, and material and manufacturing costs.

CHAPTER 3: SYSTEM AND MATERIAL EFFECTS ON THERMOELECTRIC POWER GENERATION

3.1 Introduction to thermoelectric systems

Heat losses reduce the efficiency of combustion systems. Thermoelectric modules (TEMs) operating as power generators can improve system efficiency using the waste energy available in combustion products [2, 7]. Thermoelectric generators are attractive cogeneration solutions because they are reliable, silent, and have no moving parts. Moreover, they offer the benefit of generating electricity locally at distributed combustion facilities or even household units, diminishing the need to draw power from a distant plant [95]. Extensive effort has been focused on utilizing waste heat for thermoelectric energy conversion [9, 96]. Applications include automobiles, high-temperature electronics, and gas-powered appliances used by individuals or small groups. Thermoelectric generators can also be used in systems such as water heaters in which the goal is to transfer heat energy [36, 97].

Thermoelectric materials [5] and systems with incorporated TEMs [98-100] have been previously investigated. Maximizing thermoelectric material efficiency is different than maximizing the power output of a TEM integrated into a system [8]. Extensive research has focused on improving TEM performance through the figure-of-merit, ZT $=S^2\sigma T/k$, of thermoelectric materials where S, σ, and k are the Seebeck coefficient, electrical conductivity, and thermal conductivity of the thermoelectric material, respectively. The temperature-dependent properties are evaluated at the average temperature T within the TEM. There has been considerable effort to develop phonon-glass/electron-crystal materials to reduce thermal conductivity while maintaining high values of electrical conductivity. Efforts to control the crystal structure of bulk thermoelectric materials as well as develop nanostructured materials to increase phonon scattering and improve ZT are ongoing [21]. However, maximizing Z is not necessarily the best method to optimize an entire cogeneration system. For example, combustion systems and robust electronic systems experience high operating temperatures and large temperature fluctuations, but the efficiency of many thermoelectric materials rapidly declines at high temperatures. The realization of practical, effective cogeneration

systems hinges on investigating the impact of thermoelectric material parameters coupled with system parameters.

A major challenge with system development is inefficiency caused by temperature drops at interfaces which are quantified using thermal interface resistances (TIRs) [101]. Wide temperature fluctuations, frequent thermal cycling, and large contact area in thermoelectric systems both degrade the performance of traditional thermal interface materials (TIMs) and make the module more susceptible to device failure from thermal expansion mismatch. Possible damage from thermal expansion also limits the rate of temperature change in a TEM. Nano-structured thermal interfaces, including those incorporating aligned carbon nanotubes (CNTs) or metal nanowires, may lead to improved reliability. Previous work has shown that CNT arrays may perform as an exceptional thermal interface material because they have both high thermal conductivity and mechanical compliance [102-106].

The current work estimates representative thermoelectric power generation capabilities for home water heater, automotive exhaust, and industrial furnace waste heat recovery. The goal is to compare material thermoelectric conversion to system power generation by accounting for components such as interface layers and heat exchangers. Distributed, stationary thermoelectric power generation is explored with a detailed simulation of a 15 kW, methane-fueled, tankless water heater. This work investigates TEM output when both material properties and system parameters are considered. Varying thermal interfaces and the potential of novel TIMs are presented. The limiting nature of thermal resistances in a thermoelectric cogeneration system is demonstrated, and system optimization is informed by varying parameters. The impact of thermal interface resistance on power generation efficiency is compared for water heater, automotive exhaust, and industrial furnace waste heat recovery.

3.2 Multi-system comparison

A compact, parametric system model enables a comparative analysis of three relevant thermoelectric heat recovery applications: a home water heater, an automotive exhaust system, and an industrial furnace. A home water heater represents the potential for small-scale, stationary energy harvesting. In automobiles, roughly 40% of fuel energy

is wasted as heat [107], so thermoelectric conversion of automotive exhaust heat offers an opportunity for improved fuel economy and reduced environmental impact, especially considering the scale of the worldwide automotive sector. Industrial waste heat recovery with thermoelectrics has received increasing attention since many industrial processes such as metal and glass melting discharge gas at high temperatures [108]. Thermoelectric energy harvesting offers an opportunity for energy efficiency through on-site electricity generation for these large-scale, stationary applications.

Simulation of thermoelectric systems reveals the relationship between system parameters and their impact on efficiency and power generation in these three applications. Figure 3.1 depicts a system with hot exhaust and coolant fluid streams flowing through heat exchangers surrounding a thermoelectric module. Figure 3.2 provides a thermal circuit model for the system including the temperatures of the hot gas stream and the coolant stream as nodes. Many thermoelectric system studies recognize the significant distinction between TEM conversion efficiency and overall system efficiency [35, 109]. Fewer studies consider the critical role system parameters such as thermal interface resistance, heat exchanger effectiveness, and mass flow rate play in thermoelectric power generation capabilities of combustions systems [110, 111]. A compact model assuming fixed hot and cold stream temperatures while including the impact of heat exchangers, parasitic heat loss, and interface resistance has been developed [111]. By fixing the hot and cold stream temperatures to the inlet temperatures, the spatial temperature variation along fluid flow directions is eliminated [109, 111, 112]. Although this approximation overestimates the overall temperature gradient and thus the power generation potential, this approach enables rapid multi-system comparisons.
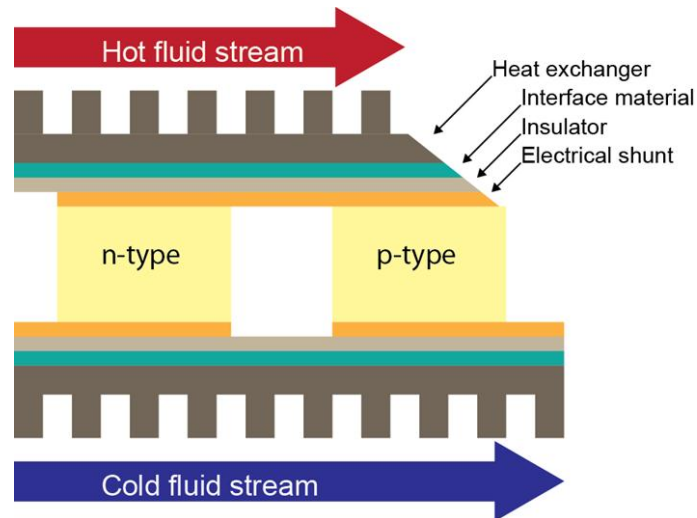
Figure 3.1: A thermoelectric system has multiple n- and p-type legs connected electrically in series with an electrical shunt material. An electrical insulator surrounds the TEM, and a thermal interface material connects the TEM to heat exchangers. Heat flows from the hot stream to the cold stream through the TEM with the thermoelectric legs connected thermally in parallel.
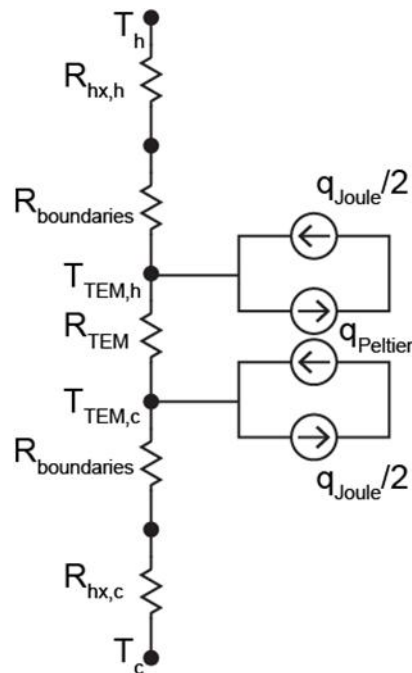
Figure 3.2: The thermoelectric system can be represented by a thermal circuit in which heat flow from the hot source through the system to the cold sink. The boundaries include conductor, insulator, and thermal interface material.

A system of equations describing the heat flow, power generation, and conservation of energy can be solved to determine conversion efficiencies. As indicated in Figure 3.2, the heat transfer through the TEM must account for Joule heating and the Peltier effect in addition to conduction through the TEM:

$$q_{Joule} = I^2 R_{TEM,e} \tag{1}$$

$$q_{Peltier} = S T_{TEM,h,c} I \tag{2}$$

$$q_{TEM} = \frac{k_{TEM} A \left(T_{TEM,h} - T_{TEM,c} \right)}{t_{TEM}} \tag{3}$$

The Peltier heat flux is dependent on the temperature of each side of the TEM. The temperature gradient through the TEM determines the electrical potential developed across it. The electrical power obtained from the TEM once it is connected to a load resistor is

$$P = I^2 R_{load} = I (S \Delta T_{TEM} - I R_{TEM,e}) \tag{4}$$

where the product of the Seebeck coefficient and temperature difference is the voltage drop. For a maximum power generation condition where the load and TEM electrical resistances are matched, the thermoelectric conversion efficiency is [111]

$$\eta_{TE,P} = \frac{P_{max}}{q_h} = \frac{S^2 \left(T_{TEM,h} - T_{TEM,c} \right)^2 \Big/ 4 R_{TEM,e}}{\left[\dfrac{\left(T_h - T_{TEM,h} \right) \left(1 - \sigma_{TE,h} \right)}{\left(\dot{m}_h C_{p,h} \varepsilon_h \left(1 - \sigma_{ex,h} \right) \right)^{-1} - R_{th,h}} \right]} \tag{5}$$

The heat flow into the TEM from the heat exchanger, q_h, shows the pertinent system parameter dependencies. An energy balance on the TEM cold side is similar for the heat flow out of the TEM, q_c, and an energy balance around the TEM shows $q_h = P_{gen} + q_c$. The terms σ_{TE} and σ_{ex} represent the fractional heat loss to the environment at the TEM and heat exchanger, respectively. These terms generally have minimal impact and are neglected here, but they can be considerable in specialized applications [13]. Thermal interface resistance R_{th} is present on both sides of the TEM where the TEM attaches to the heat exchangers. The heat exchanger effectiveness ε is obtained from ε-NTU (number of transfer units) relationships [113]. The overall system efficiency η_{sys} is the electrical power generated divided by the maximum energy that could be transferred from the hot exhaust stream.

Realistic parameters were modeled by using data reported for operation of each system: a water heater (reported here), a sports-utility vehicle [100], and an oxy-fuel glass processing furnace [108]. The parameters used in the model are listed in Table 3.1. The simulation is executed in Matlab. Temperature-dependent fluid properties at 1 atm pressure are obtained using the software Cantera. The simulation is validated with multiple conservation of energy analyses during the simulation and on the results. The tolerance allows ≤0.1% variation. When available, the effective heat transfer coefficient *UA* of the heat exchangers is used to determine heat exchanger effectiveness. It will take a number of years for thermoelectrics technology to penetrate these applications. In the meantime, thermoelectrics materials research is advancing at a rapid pace, and improved material properties are inevitable. This development was accommodated by selecting recently reported temperature-dependent property data for nanostructured PbTe [68].

The model was used to compare the difference between TEM efficiency and overall system efficiency. Ideal efficiency values are presented in Table 3.2 for the three systems indicated. The system efficiency is 32%, 33%, and 59% lower than thermoelectric conversion efficiency for the water heater, automotive exhaust, and industrial furnace applications, respectively.

Table 3.1: System specifications for simulations of three combustion systems were collected from sources providing relevant parameters. Specifications for the water heater system were obtained from communications with collaborators at Bosch RTC.

		Water heater	Automotive exhaust [100, 114, 115]	Industrial furnace [108]
Hot side	$\dot{m}$ (kg/s)	0.0041	0.01	0.03
	T_g (K)	1700	773	1033
	Gas composition (mole fraction)	CO_2: 0.16 H_2O: 0.32 O_2: 0.097 N_2: 0.42	CO_2: 0.05 H_2O: 0.05 CO: 0.002 H_2: 0.001 NO_2: 0.002 O_2: 0.01 N_2: 0.885	CO_2: 0.52 H_2O: 0.43 CH_4: 0.0019 C_2H_6: 2.0 x 10^{-5} O_2: 0.0076 N_2: 0.038
	UA (W/K)	N/A	100	250
	ε	0.85	Determined from UA	Determined from UA
Cold side	$\dot{m}$ (kg/s)	0.0125	0.1	0.1
	T_c (K)	300	360	300
	Coolant fluid	water	50/50 ethylene glycol-water mixture	water
	UA (W/K)	N/A	N/A	1800
	ε	0.99	0.99	Determined from UA

Table 3.2: Thermoelectric module and system efficiencies for three simulated combustion waste heat recovery systems were determined. Thermal interface resistance and parasitic heat loss values were omitted to obtain upper limits.

System	η_{TE}	η_{sys}	η_{sys} / η_{TE}
Water heater	4.6%	3.2%	0.68
Automobile	2.1%	1.4%	0.67
Industrial furnace	12%	4.8%	0.41

These results are promising for small-scale, distributed applications like the water heater since a reasonable efficiency is achievable. Industrial furnace exhaust heat recovery is likely to receive increasing attention since the efficiency is acceptable, and the potential to offset industrial electricity use is attractive. While the automotive exhaust

system converts the available thermal energy less effectively, consideration of only a performance analysis like this is misleading. The latter two systems benefit from economies of scale, and an evaluation of performance coupled with cost provides a more valid assessment of thermoelectric waste heat recovery potential [31, 116].

3.3 Detailed analysis of the water heater application

Efficiency improvements for appliances such as water heaters, refrigerators, and furnaces are both financially and environmentally cost-effective [117]. Deeper insight into the factors affecting thermoelectric waste heat recovery requires a more detailed analysis than the approximate calculations performed above. Such analyses have been conducted for automotive exhaust heat recovery applications [118, 119]. This approach can require detailed iterative schemes, hampering the ability to evaluate a range of parameters and compare multiple systems as accomplished above. However, it provides spatial resolution of thermal gradients which is essential for system and TEM optimization [35]. The analysis below refines the water heater system model to link thermoelectric power generation to heat transfer physics in a cross-flow heat exchanger setup.

A numerical simulation of a tankless water heater system is conducted to indicate the possibility of efficiency improvement through thermoelectric heat recovery. Also termed demand or instantaneous water heaters, tankless water heaters use a heat source to directly heat cold water without storing water in a tank and incurring energy loss [120, 121]. Figure 3.3 shows the water heater system with a fluid cross-flow arrangement through an annular-finned pipe. A water heater system has multiple pipes like the one shown. This practical heat exchanger setup is used in many applications in which cogeneration may be feasible. The thermoelectric module is modeled as a ring-shaped structure to match the pipe's shape [122]. The surface is fully covered by thermoelectric material. Optimization of fractional area coverage, or fill factor, has been investigated elsewhere [31]. The thermoelectric material is surrounded by an electrical conductor, a ceramic insulating layer, and a thermal interface material to connect the TEM to the pipe. The model accounts for external gas convection, heat generation by the TEM, and the flow rate dependence of the convection coefficients.
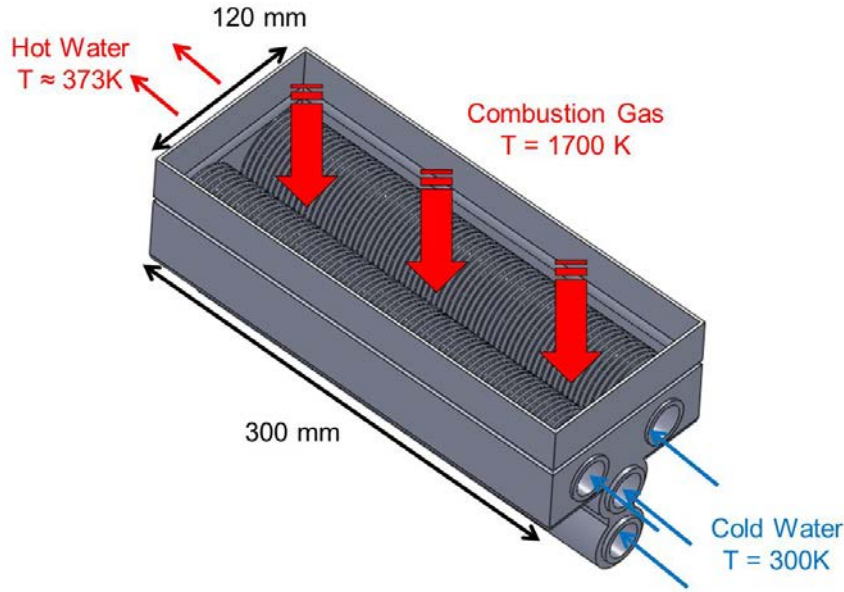
Figure 3.3: A combustion gas stream flows through a cross-flow heat exchanger to heat water in a tankless water heater system. The pipe length, inner diameter, and outer fin diameter are 300 mm, 30 mm, and 60 mm, respectively.

The external and internal convection components use empirical correlations to determine the average convection coefficients. The heat transfer from the gas stream is determined using

$$q_g = \left[\frac{1}{\eta_o h_g A} + R_{pw} \right]^{-1} \Delta T_{lm} \qquad (6)$$

to account for the effective fin efficiency of the annular pipe wall fins and the cylindrical wall conduction resistance [113]. The average gas convection coefficient is determined from a correlation for a compact heat exchanger with circular finned pipes [123]. The driving temperature difference between the gas and the pipe is approximated using a log mean temperature relationship:

$$\Delta T_{lm} = \frac{\left(T_{g,o} - T_p\right) - \left(T_{g,i} - T_p\right)}{\ln\left(\dfrac{T_{g,o} - T_p}{T_{g,i} - T_p}\right)} \tag{7}$$

Integrating the local heat transfer rate between two fluids over the total heat exchange area leads to a logarithmic relationship between the temperature differences. Modeling the temperature gradient this way allows a close approximation of the pipe wall temperature and its variation in the water flow direction without requiring a detailed solution of the temperature profile in the pipe wall along the gas flow direction. The heat transfer rate from the interior pipe wall to the water stream is

$$q_w = h_w A \left(T_{pw} - T_w \right) \tag{8}$$

where h_w is determined from the correlation for laminar internal flow [113].

The simulation results show the temperature range around the TEM is 400 K to 600 K. The chalcogenide lead telluride is an optimal thermoelectric material at these operating temperatures, so the standard properties of PbTe are used initially to explore the option of a near-term solution which does not rely on new materials development [124]. Optimal properties are selected to mimic the ability of segmented thermoelectric legs to maximize energy conversion [37]. Thermal and electrical interface resistances are neglected to ascertain upper bounds.

The simulation is conducted using a finite volume method. Each pipe is discretized in the longitudinal direction. A shooting method is used to determine the water temperature for each volume. The water temperature is assumed to be a mixed mean temperature representing the entire discrete volume. A false position or *regula falsi* method allows convergence on the amount of heat transferred to the water. Conservation of energy analyses on the results verified the simulation technique. This simulation approach is simpler than a finite element model, and it captures the significant thermal and electrical physics of the system. The approach reveals key parameters and their relative significance in system optimization.

In order to isolate the influence of system and TEM parameters, a single pipe of a tankless water heater system is simulated initially. Figure 3.4 summarizes a single pipe simulation result. In Figure 3.4a, the change in fluid temperatures demonstrates energy exchange between the hot gas and the water. The gas and the water do not reach the same temperature before the water exits the pipe, indicating additional thermal energy is available for harvesting. For cases of longer pipe length or lower water flow rate, the change in temperature with distance would decrease. The temperature drop across the TEM along the length of the pipe decreases, so the voltage developed across the TEM diminishes. In optimizing a system, the change in temperature drop indicates the thermoelectric material could vary along the length of the pipe since the thermoelectric figure of merit ZT is temperature dependent.

Figure 3.4b depicts the total electrical power from the TEM as a function of current through it. Current and load resistance are inversely related, so increasing current corresponds to decreasing load resistance. The peak power output occurs where the load resistance is equal to the electrical resistance of the TEM. The average gas outlet temperature declines as more heat energy is converted to electrical energy. The water outlet temperature changes minimally because the product of mass flow rate and specific heat capacity is larger for the water stream than the gas stream. The ability to obtain the maximum electrical power output without significantly reducing the water output temperature is promising.

Optimal system operating points are influenced by considering both conversion efficiency and relative gain in TEM power with changing load resistance. The electrical power from the TEM can be divided by the energy transferred into the system from the hot gas minus the amount of energy transferred to the water to obtain a non-dimensional power value. For a single pipe, this non-dimensional power peaks at 0.8% with an average gas outlet temperature of 1100 K indicating a significant amount of energy that can still be harvested from the gas. The voltage developed across the TEM is dropped across the TEM electrical resistance and an external load resistance. While the electrical power output comes from the voltage drop across the load resistor, the power dissipated in the TEM contributes to Joule heating and can be beneficial in this system to heat the water. The ratio of TEM power output to power dissipated decreases from an initial

amount of 21 to 1 at the matched load condition. This corresponds to an initial incremental increase in electrical power of 6.8 W/A, and the increase in power per unit rise in current declines to zero at 37 A. Because the increase in incremental TEM output power diminishes, the optimal operating point may not be at the peak power condition [111].
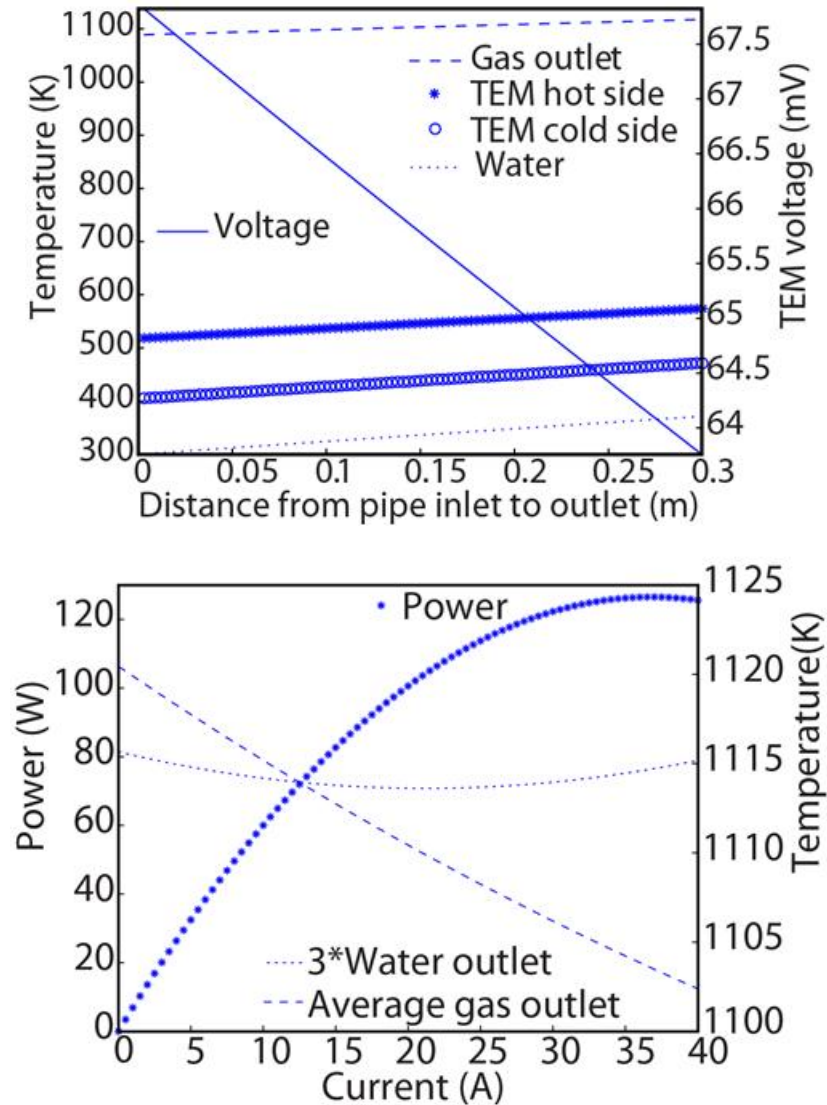
Figure 3.4: a) Fluid temperatures, TEM boundary temperatures, and TEM voltage are determined as a function of distance along the pipe. b) Electrical power output from the TEM corresponds to a change in gas and water outlet temperatures. The maximum power output for the simulated single pipe heat exchanger is 126 W.

The impact of varying system and TEM parameters are determined. Figures 3.5-3.7 demonstrate the impact of coolant flow rate, gas flow convection coefficient, and material Seebeck coefficient on the power generation potential of thermoelectric cogeneration in the water heater system. Thermoelectric power output rises as the flow rate of the water stream due to increased convective cooling of the pipe wall resulting in a larger temperature drop across the TEM. Modifying the gas convection coefficient h_g mimics multiple system variations. For example, altering fin geometry or gas flow rate will change h_g. Doubling the convection coefficient can increase the electrical power output by 50%, and the value of h_g affects the impact of the gas side convective thermal resistance relative to the other system thermal resistances. The convective resistance is often the highest heat transfer resistance [98]. This work indicates the gas side convective resistance can be comparable to TEM resistance as TEM thickness increases. The relative importance of interface resistance increases as the gas side convection improves. The limiting effect of interface materials is discussed in more detail below.

Altering the TEM thermal conductivity is an effective way to increase output power; the power is more than doubled if the thermal conductivity is reduced by 1 W/m-K. Of all the parameters considered, thermal conductivity improvement results in the largest gain in power output. The top axis in Figure 3.8 shows ZT corresponding to varying thermal conductivity with all other properties held constant. The maximum operating temperature of the thermoelectric material must be considered in evaluating the ZT and selecting TEM materials. For example, Bi_2Te_3 has a maximum operating temperature of about 550 K and could not be considered for this application.
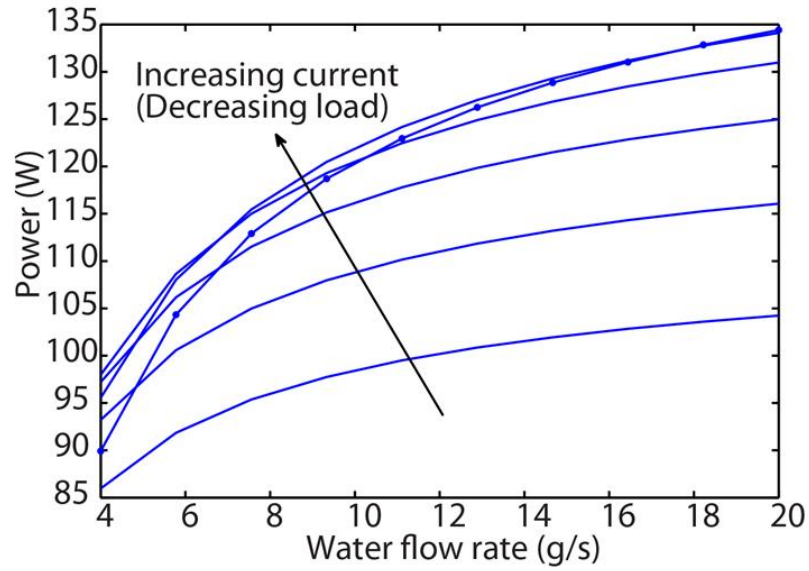
Figure 3.5: Thermoelectric power output rises at a declining rate as the flow rate of the water stream increases. The rise is due to increased convective cooling of the pipe wall resulting in a larger temperature drop across the thermoelectric module. The relative impact of reducing the thermal convection resistance decreases, and the energy transfer within the water dominates.
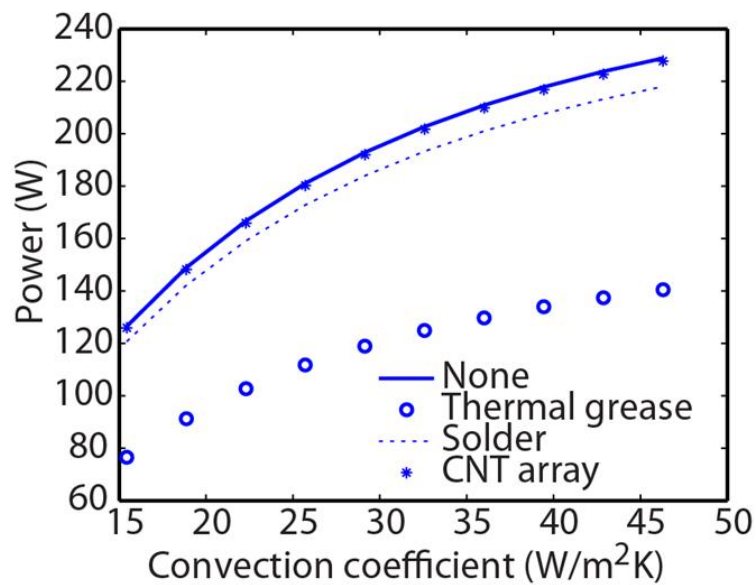
Figure 3.6: Modifying the gas convection coefficient h_g mimics multiple system variations. Doubling the convection coefficient can increase the electrical power output by 50%, and the value of h_g affects the impact of the gas side convective thermal resistance relative to the other system thermal resistances. Altering fin geometry or gas flow rate will change h_g. There is uncertainty around the value of h_g because it is highly dependent on flow properties and system geometry, and the empirical correlation used is only the best available approximation to the geometry considered.
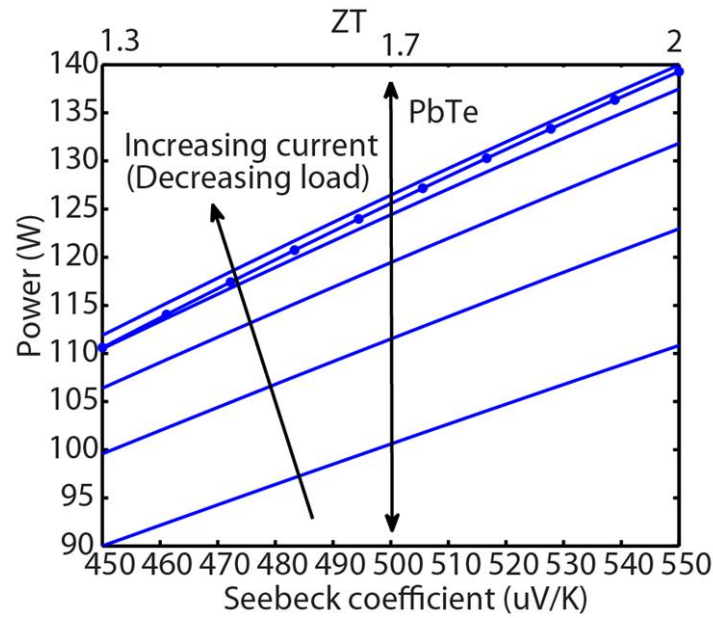
Figure 3.7: Increasing the Seebeck coefficient by 100 uV/K augments the power generation by 19 W. Significant increases in Seebeck coefficient have been achieved by creating a large change in the density of states near the Fermi level [84]. Stable, scalable materials demonstrating this enhancement of thermopower must still be demonstrated [7].
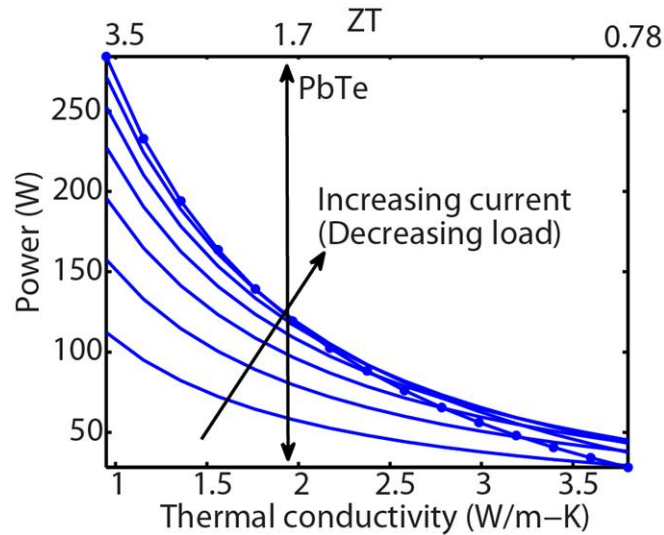
Figure 3.8: TEM electrical power output increases significantly as thermoelectric material conductivity decreases. Optimized materials are simulated by holding the other material properties constant. The curve for the lowest load resistance has markers to guide the eye.

The maximum electrical power output depends on the configuration of the heat exchanger system. Options for pipe configurations in the water heat system are considered in Table 3.3. The table provides the incremental gain in adding pipes in multiple configurations. Pipes located next to each other horizontally are in a parallel thermal connection whereas vertically stacked pipes are in a series thermal connection. The gas outlet temperature is indicative of the amount of energy remaining in the gas stream after it has passed over all of the pipes. Because the gas stream temperature drops as it passes over the pipes, the electrical power out of a pipe's TEM decreases as it is stacked lower in a vertical arrangement. However, increasing the number of pipes stacked horizontally would also require an increase in the mass flow rate of the gas stream. Additionally, the average temperature across the TEM is significantly different in each pipe, so different thermoelectric materials should be considered. The TEM material in each pipe should have a peak *ZT* for the operating temperature of that pipe.

Table 3.3: Systems configurations can vary to connect pipes thermally in parallel and series. TEM electrical output increases most for parallel arrangements at the cost of higher gas flow rates.

Pipe configuration	Diagram of cross-section	Peak power output (W)	Gas outlet temperature (K)	Thermal connection
Single		250	1100	2 pipes in parallel
4 horizontal, stacked		340	740	2 parallel sets with 2 in series
6 horizontal, stacked		370	530	3 parallel sets with 3 in series
4 horizontal *requires higher gas flow rate		500	1100	4 in parallel

3.4 Impact of thermal interfaces

Estimating the thermal resistance of interface materials is a major challenge for this work. Interface materials from thermal greases to metallic alloys have thermal conductivities ranging from 0.2 to 50 W/m-K [125]. In modern computers, these materials have thicknesses between 20 and 100 µm, yielding total thermal resistances from 150 to 0.6 m^2K/MW. In macroscale systems such as a water heater the thicknesses of interface materials can be substantially larger. The large thickness is owed to geometrical inconsistencies in the larger components as well as the requirement for the interface to overcome thermomechanical mismatch between the adjacent materials. In contrast to computers, which are subjected to a temperature variation of approximately 100 K, combustion-based TEM systems could experience thermomechanical cycling up to 600 K. For the present work, we assume a TIM thickness of 1 mm and thermal conductivities of 1 W/m-K for grease, 10 W/m-K for metal solder, and 100 W/m-K for a novel CNT-based interface material [103, 105].

The degree to which thermal interface resistance degrades system efficiency depends strongly on thermoelectric thickness. Figure 3.9 illustrates a thicker TEM raises the TEM thermal resistance and thus the temperature drop across it. A 22 W/mm improvement in power is possible. The thermal interface material strongly reduces the output power and severely affects power output as TEM thickness increases. Particularly for TEMs composed of novel thin film materials, power generation capability will be limited by the heat sink and TIM thermal resistances, and thermal resistance matching between these system elements and the TEM is critical [126].
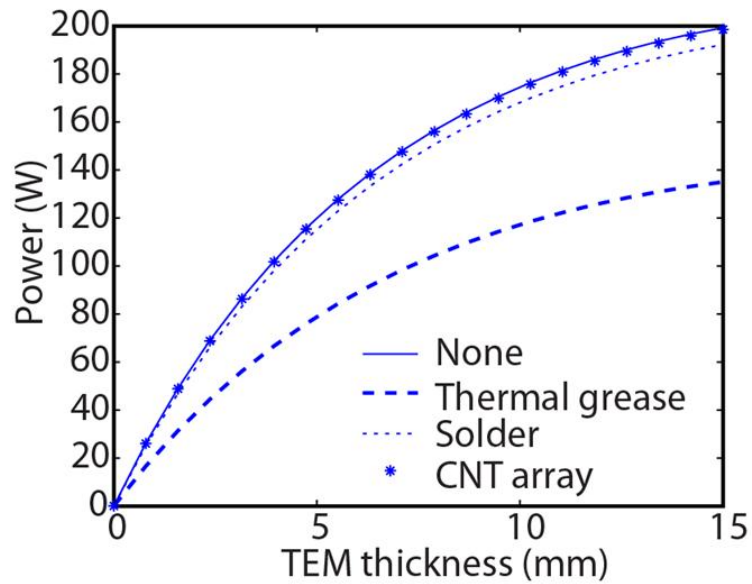
Figure 3.9: TEM electrical power output increases with TEM thickness, but interface materials can severely limit the gain in power output. An interface material thickness of 1 mm is used for the simulation.

As shown in Figure 3.1, there are two thermal interfaces, one on each side of the thermoelectric module. Hot side TIR is higher than cold side TIR in practical systems, so the analysis is extended to account for $R_{th,h}$ equal to and multiple factors larger than $R_{th,c}$. The values of $R_{th,c}$ shown in Figure 3.10 correspond to TIMs with thermal conductivity from 1 to 100 W/m-K, and the solid line shows the maximum operating point with no TIR.
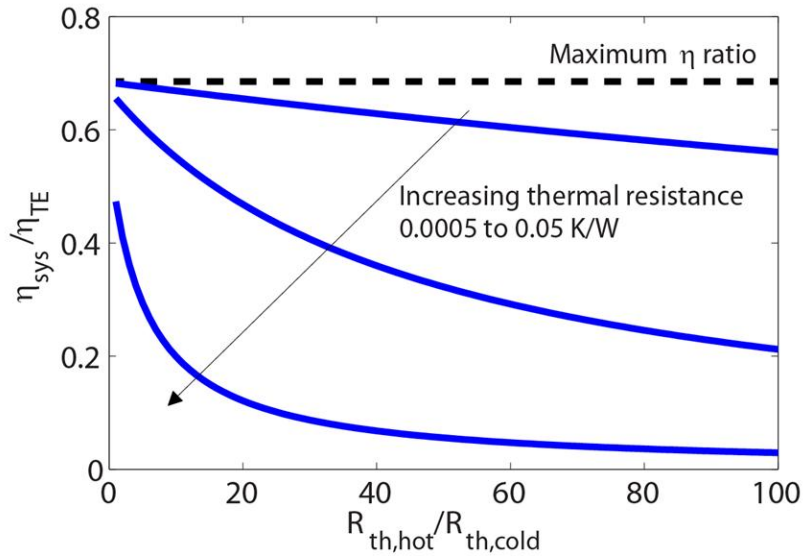
Figure 3.10: The ratio of system to module thermoelectric conversion efficiency is compared to the ratio of hot side to cold side thermal interface resistance for the water heater system. The efficiency reduction decreases as the thermal interface resistance decreases.
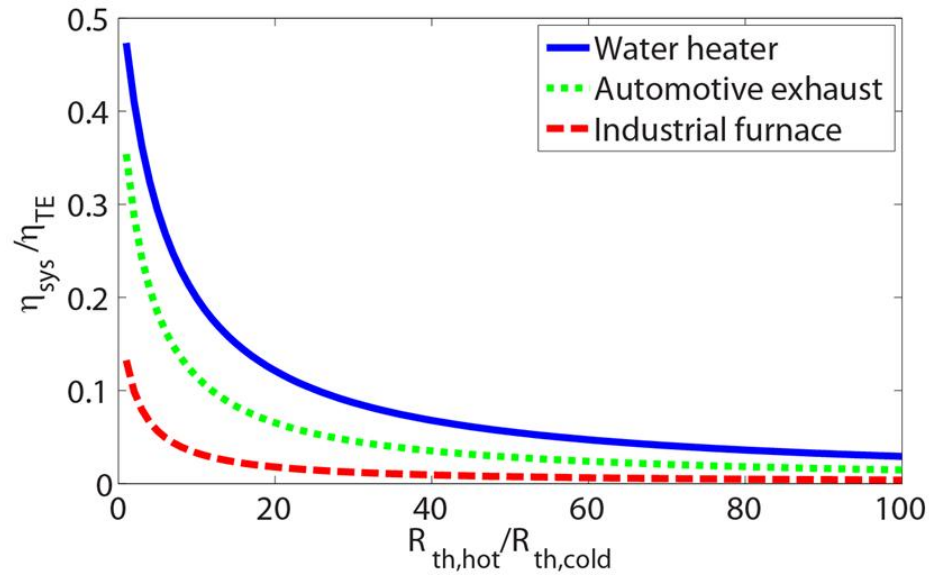
Figure 3.11: The ratio of system to module thermoelectric conversion efficiency is compared to the ratio of hot side to cold side thermal interface resistance for the three combustion systems. The relationship can be fit to an exponential decay to characterize the efficiency reduction due to the interfaces. $R_{th,c}$ is held constant at 0.05 K/W.

The severe degradation in power generation potential due to thermal interface resistance is not limited to appliance-type systems like the water heater. Figure 3.11 illustrates the impact of TIR for all three applications: water heater, automotive exhaust, and industrial furnace. The relationship between the efficiency and TIR ratios is of the form

$$\frac{\eta_{sys}}{\eta_{TE}} = ae^{b\left(R_{th,h}/R_{th,c}\right)} + ce^{d\left(R_{th,h}/R_{th,c}\right)} \tag{9}$$

where $a, b, c,$ and d are coefficients dependent on $R_{th,c}$. Table 4 provides the coefficients corresponding to the relationships shown in Figure 3.11. The form of the relationship is the same for varying cold side TIRs, but the coefficients in the fitting relationship change as cold side TIR and the corresponding TIR ratio change.

Table 3.4: Coefficients for the relationship between conversion efficiency and the ratio between hot and cold side thermal interface resistances were determined using a fitting analysis. Fitted values presented here are for a system with 0.05 K/W cold side thermal resistance.

	a	b	c	d
Water heater	0.37	-0.15	0.14	-0.018
Automotive exhaust	0.31	-0.21	0.089	-0.021
Industrial furnace	0.13	-0.28	0.029	-0.025

This analysis provides rapid assessment of TIM system-level impacts. It is much easier to measure the effective TIR for TIMs at lower temperatures. Experimental setups to measure TIMs at high temperatures (e.g. exhaust stream temperatures of these systems) are rare and challenging to develop [127]. Using this analysis, an easily obtained value of $R_{th,c}$ can be combined with an estimate of the relative $R_{th,h}$ value to determine the effects of system efficiency reduction due to thermal interface resistances.

The difference between thermoelectric material conversion efficiency and system-level power generation in three combustion applications is determined. A tankless water

heater system with an integrated thermoelectric module is numerically simulated in detail to investigate the impact of varying both system and TEM parameters. Reducing the TEM thermal conductivity by 50% doubles the electrical power output. Increasing the hot side convection coefficient and increasing the TEM thickness can increase the output power by up to 50%. Thermal interface materials significantly limit the ability of a TEM to maximize output in a cogeneration system. Industry standard TIMs can reduce TEM power output by approximately 40% depending on material and thickness. More work is needed to minimize this thermal resistance while accounting for the severe repetitive thermomechanical cycling in these systems. The current work suggests that novel interfaces such as those based on CNT technology are encouraging options for future research. Thermoelectrics offer a promising cogeneration opportunity, and enhancements in TEM materials will improve the technology's potential. Recognizing and solving the remaining challenges of TEM system integration are required to improve overall system efficiency and power output.

CHAPTER 4: ELECTROTHERMAL PHENOMENA IN ZINC OXIDE NANOWIRES AND CONTACTS

4.1 Introduction to electrothermal nanowire phenomena

Nanowires are promising for applications including transistors [128, 129], sensors [130, 131], and energy conversion devices [132]. Recent research examined their potential in energy applications including thermoelectric waste heat recovery [133, 134], solar cells [135], and batteries [136-138]. Zinc oxide nanostructures have generated particular interest due to their optical and electrical properties, ease of synthesis, and non-toxicity [139-141]. Most ZnO nanowire devices use electrical contacts where the contact composition and transport of energy carriers are critical for performance [142]. Contacts can dominate nanowire device response, particularly in devices exhibiting rectifying behavior [143, 144].

Nanoscale thermal contact resistance has been studied for nanowires and nanotubes. Using a contact resistance model based on acoustic mismatch theory [145], the thermal resistance of a nanowire point contact and variations in phonon transmission through welded and non-welded nanowire contacts were determined for indium arsenide nanowires [146]. Heat generation and thermal failure limit the reliability of nanowire/nanotube devices [147, 148]. Heat generation and electrical breakdown studies on individual carbon nanotubes show failure often occurs in the interior, away from contacts [148]. There is a pressing need for a methodology determining the impact of heat generation in nanowire devices, particularly those which may have limited electrode contact area and interfacial layers. The need is significant for oxide nanowires such as ZnO, SnO_2, and MgO in which the nanocontact interfacial effects increase the effective contact resistance [149].

This work analyzes heat generation within a nanowire and at its contacts, and the relative heat generation is used to determine nanowire device limitations. The model is applied to ZnO nanowires fabricated here using solution-synthesis [150]. Data for ZnO, GaN, and Si nanowire structures measured by other researchers are utilized to determine the relative heat generation for a broader range of materials.

4.2 Electrothermal model of a single nanowire structure

The model considers a nanowire contacted by two metal electrodes as shown in Figure 4.1a with current flowing through the structure. The simplified one-dimensional heat diffusion equation

$$k_w A \frac{d^2 T}{dx^2} + \rho_w A J^2 - g(T - T_o) = 0 \qquad (1)$$

neglects the temperature dependence of both thermal conductivity and thermal conductance from the nanowire to the substrate. The parameters k_w, ρ_w, A, and T are the nanowire thermal conductivity, resistivity, cross-sectional area, and local temperature, respectively. The first term quantifies heat diffusion along the nanowire; the second term accounts for Joule heating within the nanowire due to current density J flowing through it. Thermal boundary conductance g is used to calculate the rate of heat loss per unit length to the underlying substrate at ambient temperature T_o. By linearizing the relationship between the nanowire-substrate heat conduction with respect to the temperature difference, this analysis may overestimate the peak temperature distribution in the nanowire by up to 15% for temperature differences exceeding 1000 K. Other complications reduce the accuracy for the case of extreme temperature differences, including the temperature dependent thermal conductivity and nanowire-metal electrical and thermal contact resistances, which renders this approach approximate and best suited for scaling assessment. One-dimensional conduction is assumed, and temperature variations in the nanowire and electrode cross-sections are neglected. The resistance to heat conduction inside the nanowire and electrode cross-sections is several orders of magnitude smaller than the thermal resistance of their surroundings, so the 1D approximation is valid [113].

Heat generation occurs at the electrode-nanowire contact due to electrical contact resistance. The model is applied to Ohmic contacts in which the metal work function is smaller than the semiconducting nanowire electron affinity, and the current-voltage relationship is linear. This condition does not preclude analysis of metal-nanowire contacts with interfacial layers so long as the barrier width is thin enough to fulfill the

Ohmic contact requirement. The representation of electrical contact resistance for Schottky contacts [151] is not valid in this approach because it applies only near zero bias condition and does not describe the barrier to charge carrier transport resulting in heat generation.
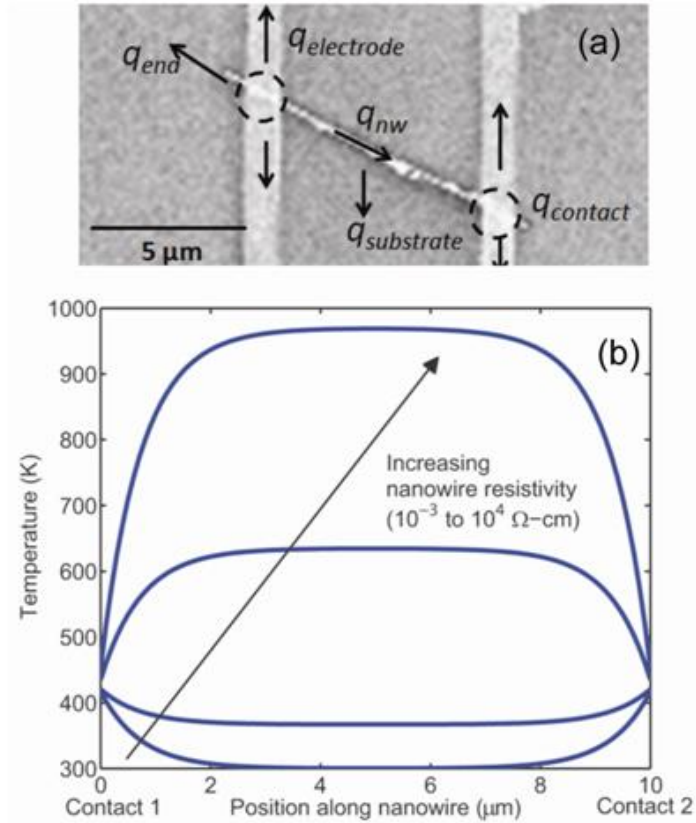
Figure 4.1: (a) Scanning electron micrograph of a nanowire device with labels indicating heat conduction and generation. Metal-nanowire contacts are circled. (b) Temperature profiles obtained by applying the electrothermal analysis to a ZnO nanowire structure with metal contacts. The parameters used to generate the profiles are $k_w = 20$ W/m-K, $r = 80$ nm, $L_w = 10$ μm, $\rho_c = 5 \times 10^{-3}$ Ω-cm^2, $g = 1.2$ W/m-K and $I = 400$ nA. The resistivity range is representative of ZnO nanowires measured by other researchers [152].

Research on thermal contact resistance between a nanowire and an underlying substrate provided a theoretical framework for determining this thermal resistance based on van der Waals interactions between the two surfaces [153]. An extended model

55

accounting for ballistic and diffusive phonon transport through a nanoscale constriction was developed along with the effective reduction in fluid thermal conductivity due to the small gap between the nanowire and substrate [154]. Both approaches have been applied to experimental characterization of a carbon nanotube with the extended model predicting a value closer to the one deduced from experiments [155]. The phonon mean free path in ZnO is approximately 30 nm; the contact width between the nanowire and substrate is 2 nm for nanowires analyzed here. While the contact is smaller than the phonon mean free path, the substrate is a 200 nm layer of SiO_2 on silicon, so transport across the interface is treated as diffusive. Thermal constriction resistance R_c to a substrate with thermal conductivity k_s is [153]

$$R_c = \frac{1}{L_w}\left[\frac{1}{\pi k_w}\ln\left(\frac{2D}{w}\right) - \frac{1}{2k_w} + \frac{1}{\pi k_s}\ln\left(\frac{D}{\pi w}\right)\right] \quad (2)$$

where L_w, D, and w are the nanowire length, diameter, and the half-width of its contact with the substrate, respectively. The effective thermal resistance R_f of the fluidic gap between the nanowire and substrate is [154]

$$\frac{1}{R_f} = 2L_w k_f \int_w^{D/2} \frac{dy}{D/2 - \sqrt{D^2/4 - y^2} + 2a\lambda_f} \quad (3)$$

where a is 2 for an air gap at room temperature, k_f is the thermal conductivity of the fluid, and λ_f is the mean free path of air molecules. This expression for R_f is determined using the reduction in the effective thermal conductivity of the air since the thickness of the fluidic gap is comparable to the mean free path of the air molecules. As a result, the thermal resistance of the fluidic gap is approximately 2 x 10^7 K/W which is orders of magnitude larger than the thermal constriction resistance of 4 x 10^4 K/W. The total thermal resistance R_t is $R_t = (R_c R_f)/(R_c + R_f)$. The heat loss g is the inverse of this thermal resistance divided by nanowire length.

The model yields the temperature profile of a nanowire with contacting electrodes. Figure 4.1b demonstrates the results for a nanowire device where symmetric contact heat generation is assumed. Asymmetric contact heating could occur in rectifying systems with Ohmic and Schottky contacts. The temperature distribution depends strongly on nanowire electrical resistance as demonstrated by the case where the large nanowire resistivity leads to a peak device temperature within the nanowire. Several researchers have conducted experiments using the resulting nanowire/nanotube failure to characterize the nanostructure's properties [147, 156]. Nonetheless, there is another critical failure mode in which metal-nanowire contact resistance dominates.

4.3 Electrothermal analysis of zinc oxide nanowires

The electrothermal model is applied to measurement structures of 1% Ga-doped ZnO nanowires with Ti/Ag electrodes. The nanowires were solution-synthesized and single crystalline wurtzite in structure [150]. A dilute nanowire solution was dispersed on a silicon substrate topped with 200 nm SiO_2. Electrodes were patterned on nanowires with electron beam lithography as shown in Figure 4.2; atomic force microscopy was used to verify electrode thickness. Images obtained with an FEI XL30 Sirion scanning electron microscope (SEM) enabled extraction of nanowire and electrode dimensions. A Keithley 2612 measured current and voltage to provide electrical resistance.

Unique precautions are required for individual nanowire measurements [157]. Stray voltages, even at low levels, can easily damage the nanowire or contact electrodes. Hence, all the electrical probes were shorted and connected to the ground potential before putting the probes in contact with the microfabricated measurement structure. Additionally, the nanowire structure is a high impedance load, so measurements were conducted by sourcing voltage and measuring current. Particularly for the highly variable nanowire contact conditions, this is the safest method to protect the device under test. Finally, all measurements were conducted inside a Faraday cage.

The selection of the metal electrode material contacting the semiconducting nanowire is important. In some cases, Schottky contacts can form when the metal's work function is larger than the semiconducting nanowire's electron affinity. Given the altered surface state on the nanowires, the electron affinity may be different than the nominal value.

Even when a low metal work function is used as an intermediate layer between the nanowire and a higher work function metal, Schottky contacts can form. Additionally, surface defects may pin the Fermi level to a non-nominal value. It is particularly important to isolate a device with Schottky contacts from any light source since the structure will operate as a Schottky contact solar cell. Furthermore, ZnO exhibits persistent photoconductivity. The incident energy from the light will alter the nonlinear current-voltage relationship. Nanowire structures with Ti/Au electrodes had Schottky contacts which resulted in combined thermionic and field emission, or tunneling, as the dominant current transport process through the Schottky contacts [158] where the relationship between current and voltage is nonlinear [143, 151, 159-161]:

$$\ln(I) \propto V\left(\frac{q}{k_b T} - \frac{1}{E_o}\right) \tag{4}$$

The parameter E_o is related to the transparency of the barrier to electron flow E_{oo}:

$$E_{oo} = \frac{q h_p}{2}\sqrt{\frac{N}{m_{eff}\varepsilon_s}} \tag{5}$$

where N, m_{eff}, ε_s are the doping concentration, carrier effective mass, and permittivity of the semiconducting nanowire, respectively. This nonlinear current-voltage relationship from the back-to-back Schottky contact devices enabled extraction of a nanowire doping concentration of 10^{18} cm^{-3}. Given the variability of the nanowire surface and the contacts made to it, verifying the doping concentration using another method is advisable.

For the Ohmic contact devices with Ti/Ag electrodes, a transmission line analysis yields specific contact resistivity of the metal-nanowire contact [162-164]. The electrical contact resistance R_m between the metal and the nanowire is [162, 164]

$$R_m = \frac{\rho_c}{2\pi L_T F}\coth\frac{L_m}{L_T}. \tag{6}$$

L_T, the electrical transfer length [162, 164]

$$L_T = \sqrt{\frac{r\rho_c}{2F\rho_w}} \qquad\qquad (7)$$

relates nanowire resistivity ρ_w to specific resistivity of the metal-nanowire contact ρ_c. The fraction of nanowire circumference covered by metal is F for a nanowire with radius r; the length of contact is L_m. SEM imaging of the structures tilted at various angles show the majority (~75% or more) of the nanowire circumference is covered by metal. Full coverage ($F = 1$) is assumed, providing an upper-bound on ρ_c. The total resistance between two contacts is $R_T = 2R_m + (\rho_w/\pi r^2)L_w$. A 4-point measurement reveals nanowire resistivity which is used with 2-point measurements to determine contact resistance. Surface depletion is neglected; the analysis assumes the entire nanowire cross-section is used for electrical conduction. This assumption is validated by a calculation of the depletion width which is less than 3 nm, less than 5% of the radius [165].

Nanowire and specific contact resistivity for two structures are listed in Table 4.1. There are two possible reasons the extracted contact resistivity spans multiple orders of magnitude. Solution-synthesized nanowires often have a surfactant coating remaining on the nanowire surface. Raman spectroscopy on the same batch of nanowires measured here shows evidence of the surfactant [166]. Multiple 4-point measurements were performed on sample 2 before the 2-point measurements. It is possible one of the electrode-nanowire contact areas decreased during the measurement. In this case, the actual contact resistivity would be lower than the value calculated using the contact area determined from pre-measurement SEM images.

Table 4.1: ZnO nanowire parameters determined here from 4- and 2-point measurements.

Sample	r (nm)	ρ_w (Ω-cm)	ρ_c (Ω-cm^2)
1	52	4.7×10^{-3} ($\pm 2.4 \times 10^{-3}$)	5.4×10^{-4} ($\pm 1.3 \times 10^{-4}$)
2	67	1.0×10^{-2} ($\pm 1.4 \times 10^{-2}$)	17 (± 12)

Incorporating experimental nanowire and contact resistivity values into the electrothermal model indicates the peak temperature rise occurs at the metal-nanowire contact. At the maximum measured current of 5 µA, the predicted contact temperature is 900 K which approaches the silver electrode melting point. Shown in Figure 2, post-measurement images show device failure at the metal contact while much of the nanowire between the electrodes remains intact. The images reveal pitting of the metal at the contact resulting in reduced contact area between the nanowire and electrode. The pitting may be due to current crowding at the leading edge of the metal-nanowire contact region [167]. The localized region of high current density at the leading edge may exacerbate electromigration of the metal electrode. Therefore, the actual contact area between the electrode and nanowire is less than the nominal value causing an increase in current density and contact temperature as shown in Figure 3. Failure of the device occurs at one contact indicating the contact resistances are asymmetric. Though challenging due to the rapid evolution of dimensional changes from heat generation, an informative future study would involve *in situ* imaging of the nanowire structure during the electrical measurement to capture the dynamic change in electrode width.
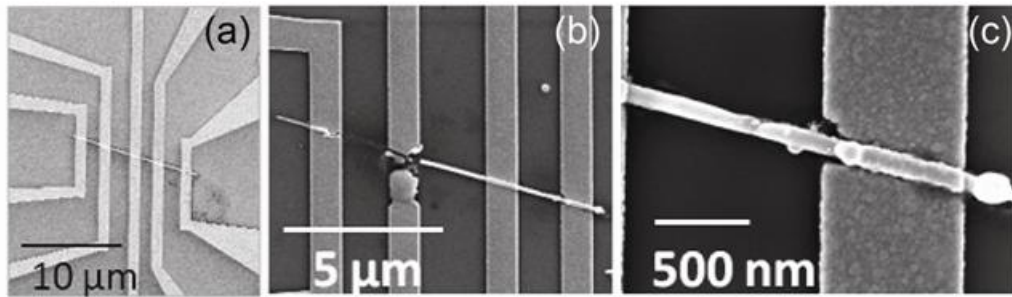
Figure 4.2: Scanning electron microscope image of ZnO nanowire device (a) before and (b & c) after measurement. There is pitting of the contact where the effective electrode width and area of contact with the nanowire decrease, and the metal electrode melts. The rightmost electrode shown in (a) was not used for measurements presented here.
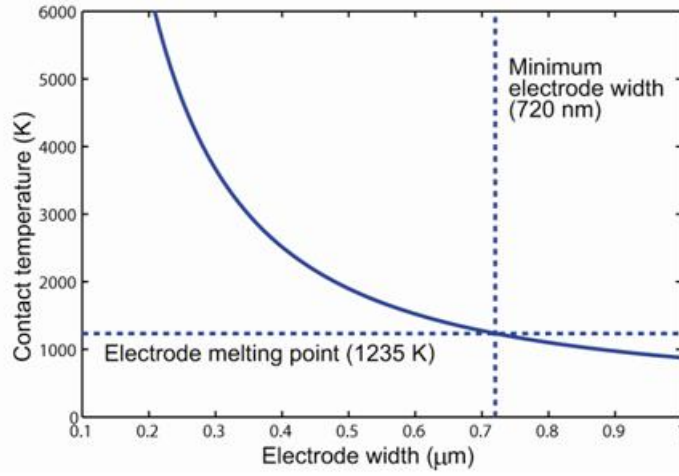
Figure 4.3: Peak contact temperature changes with electrode width. The minimum width the ZnO nanowire device can tolerate is 720 nm; further electrode narrowing causes the contact to reach the electrode melting point.

4.4 Development and application of a relative heat generation metric

Analysis of nanowire structure failure is critical to the development of reliable devices. It is useful to compare heat generation in the nanowire divided by heat generation at the contacts. For Ohmic contacts and device current I, this non-dimensional, relative heat generation is represented as $\theta = I^2 R_w/(I\Pi + I^2 R_w)$ which can also be expressed as

$$\theta = \frac{J\rho_w L_w}{\pm\frac{1}{e}\left[(E_C - E_F) + Ck_bT\right] + J\rho_w L_T \coth(L_m/L_T)} \qquad (8)$$

where E_C and E_F are the semiconducting nanowire conduction band edge and Fermi level, respectively. The parameter C in the Peltier coefficient Π depends on the variation of the density of states and mobility with electrical energy [168]. The numerator represents nanowire Joule heating. The denominator has two components contributing to contact heating, the Peltier effect and the power dissipated due to electrical contact resistance. The sign of the Peltier term depends on the direction of current through the

metal-nanowire contact where one contact has a positive Peltier heat release term while the other has a negative heat absorption term. The relative heat generation θ thus indicates where nanowire device failure is likely. Figure 4.4 shows the relative heating as a function of contact resistivity for the wide range of ZnO nanowire contact resistivity [169]. As effective contact resistance of the junction increases, or nanowire resistivity decreases, the device is more prone to fail at the contact.
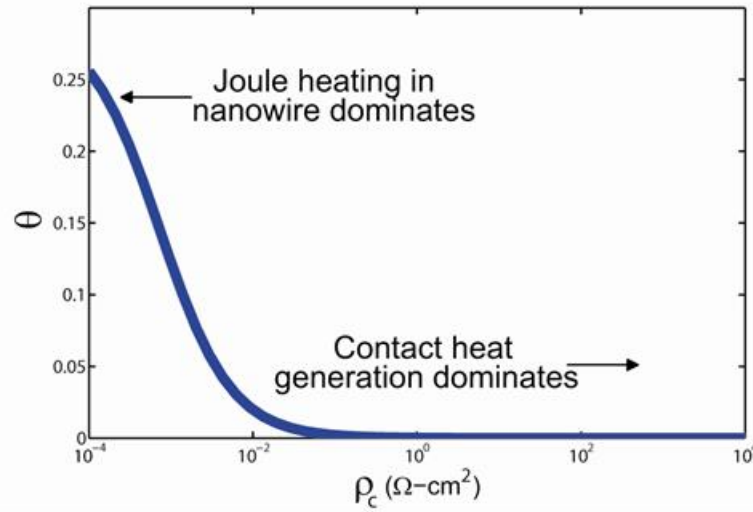
Figure 4.4: Ratio, θ, of the heat generation rate in the nanowire to the heat generation at the contacts varies with electrical contact resistivity of the metal-nanowire contact and indicates the likely device failure point. The figure shows the variation in θ for a ZnO nanowire device operating at 1 μA for which the Peltier coefficient is evaluated at the contact temperature determined from the electrothermal model. The parameters used are $\Pi = 0.17$ V, $r = 66$ nm, $L_w = 7$ μm, $\rho_w = 1 \times 10^{-2}$ Ω-cm.

Electrothermal transport data for relevant materials are examined to assess the impact of relative heating on an array of nanowire devices proposed for energy conversion applications. Figure 4.5 shows the relative heating versus specific contact resistivity for silicon [162, 170-174], gallium nitride [164, 175-178], and zinc oxide [129, 179-181]. Using data reported by previous studies, the relative heat generation rate is determined assuming typical metal-nanowire contact length, nanowire length, and device current of 1

μm, 10 μm, and 1 μA, respectively. The electrical transfer length is calculated assuming full metal coverage ($F = 1$). When not reported, nanowire radius is measured from the authors' presented SEM images using an image analysis program. If authors report carrier concentration and mobility from 4-point measurements, nanowire resistivity is calculated. The Peltier term is several orders of magnitude less than heating from contact resistivity, so this term was neglected in calculations for the data in Figure 4.5.
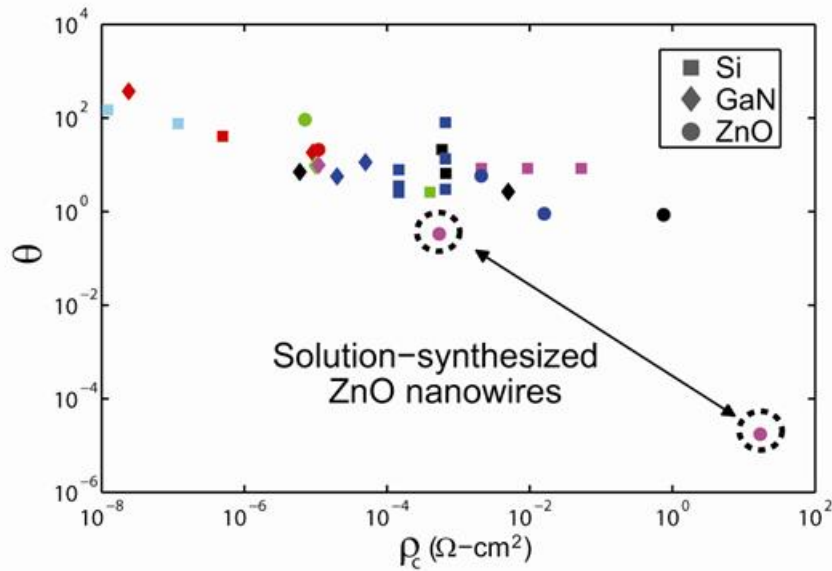
Figure 4.5: The ratio of nanowire-internal to contact heat generation plotted as a function of reported contact resistivity for Si (■), GaN (◆), and ZnO (●) nanowire devices from various studies (Si [162, 170-174], GaN [164, 175-178], ZnO [129, 179-181]). Nanowire material type is designated by marker type. Data from each source are differentiated by color as indicated in the references. Data from this work are circled.

The comparison of multiple nanowire devices demonstrates a wide range of specific contact resistivity, approximately 1.2×10^{-8} to 0.75 Ω-cm^2. Likewise, the relative heating parameter for devices other than the solution-synthesized ZnO nanowires spans two orders of magnitude. ZnO nanowire structures with relative heating parameters below 0.1 where contact heating dominates will likely fail during device operation due to melting of the metal contact. Little information is reported for such failures, rendering a

thorough analysis of experimental electrothermal phenomena in nanowire devices difficult. The necessity of such communication is highlighted by this analysis. The paucity of such data for solution-synthesized nanowires is significant. With the exception of data reported here for ZnO, the data used to generate Figure 4.5 are taken from measurements of vapor-synthesized (e.g. chemical vapor deposition, vapor-liquid-solid growth) nanowires. Ease of fabrication makes solution-synthesized nanowires promising, but contact resistivity may limit their functionality and impact device performance. Annealing processes to eliminate residual surfactant are particularly limited with ZnO nanowires since an insulating oxide readily forms at the nanowire-metal contact for multiple metals, a process that can be amplified with elevated temperatures. Annealing of these solution-synthesized ZnO nanowire structures with Ti and Ti/Al electrodes showed a reduction in electrical conductivity.

This work proposes an electrothermal model which links current-voltage measurement data to the resulting temperature profile of semiconducting ZnO nanowire devices. The contact resistance of the metal-semiconductor contact leads to heat generation at the contact which surpasses the nanowire Joule heating. Therefore, the contact heat generation limits the operating range of the nanowire device. This approach is used to determine design and operating parameters for nanowire devices. Additionally, recent reviews demonstrate the substantial variability in ZnO nanowire devices, particularly at the metal-semiconductor contacts. This work highlights the significance of these contacts and the need for further contact characterization and improvements.

CHAPTER 5: CONCLUSION

Global energy demand will increase dramatically over the coming decades. Fulfilling these energy needs will require new technological advancements. The technological challenges encountered during this process can be overcome by understanding the interlinked relationships between enabling materials, energy system design, and techno-economic analyses. This doctoral research has demonstrated these relationships as applied to thermoelectric energy conversion devices, a promising technology for waste heat recovery and energy efficiency improvements.

A thermo-economic analysis integrated materials and manufacturing costs and state-of-the-art materials performance to evaluate current thermoelectric technology and identify future development targets. An energy system analysis yielded a thermoelectric system modeling tool and demonstrated the impact of system and material parameters on the power generation capability of practical systems. A study of a novel zinc oxide nanowire material provided an electrothermal model and relative heat generation metric which demonstrated the impact of nanowire contacts on characterization and devices.

The nanoengineering of materials enables tunable properties which can enhance energy conversion processes and systems, and, indeed, research developments indicate promising properties for nanostructured materials. However, the role materials like nanowires and nanotubes will play in energy conversion advancements remains ambiguous. As the nanowire contact study described here demonstrates, accessing the enhanced nanomaterials properties requires excellent contact to nanostructured materials and often individual nanostructures like nanowires. The interaction between the nanoscale realm in which the property enhancement is created and the macroscale world is perhaps the greatest barrier to the proliferation of nanoengineered materials for energy conversion applications. A key remaining scientific and engineering challenge is to realize the nanoscale benefits in macroscale systems.

The synthesis and manufacturing of nanostructured materials, particularly nanowire materials, are crucial factors in the development of nanomaterials for energy conversion. The scalability and cost of these processes is often not addressed amidst the clamor over the promise of these novel materials. Nonetheless, scalability, throughput, and cost are

critical parameters for the development and commercialization of practical components and systems. The techno-economic analysis provided here for thermoelectric applications demonstrates the significant challenges which remain on this front. The manufacturing techniques traditionally associated with nanomaterials are still relatively expensive which makes these materials less competitive from a cost-performance perspective. New synthesis and manufacturing techniques like solution synthesis and spray coating will greatly evolve the deployment of nanomaterials with enhanced, tunable properties.

The rapid research progress in synthesis and characterization of nanowire materials promises opportunities for transformative energy conversion technologies. The remaining challenges of integrating nanotechnologies into macroscale systems and creating economically viable devices pose the most pressing obstacles to overcome. Future work on these topics would be valuable and timely.

REFERENCES

[1] *World Energy Outlook 2011*. Paris, France: OECD/IEA, 2011.

[2] M. Zebarjadi, K. Esfarjani, M. S. Dresselhaus, Z. F. Ren, and G. Chen, "Perspectives on thermoelectrics: from fundamentals to device applications," *Energy & Environmental Science,* vol. 5, p. 5147, 2012.

[3] "Advanced Manufacturing Office," U. S. D. o. Energy, Ed., ed.

[4] "Annual Energy Review," U. S. E. I. Administration, Ed., ed, 2010.

[5] A. Shakouri, "Recent Developments in Semiconductor Thermoelectric Physics and Materials," *Annual Review of Materials Research,* vol. 41, pp. 399-431, 2011.

[6] J. R. Sootsman, D. Y. Chung, and M. G. Kanatzidis, "New and old concepts in thermoelectric materials," *Angew Chem Int Ed Engl,* vol. 48, pp. 8616-39, 2009.

[7] T. M. Tritt, "Thermoelectric Phenomena, Materials, and Applications," *Annual Review of Materials Research,* vol. 41, pp. 433-448, 2011.

[8] G. J. Snyder and E. S. Toberer, "Complex thermoelectric materials," *Nature Materials,* vol. 7, 2008.

[9] L. E. Bell, "Cooling, heating, generating power, and recovering waste heat with thermoelectric systems," *Science,* vol. 321, pp. 1457-61, Sep 12 2008.

[10] M. S. Dresselhaus, G. Chen, M. Y. Tang, R. G. Yang, H. Lee, D. Z. Wang, Z. F. Ren, J. P. Fleurial, and P. Gogna, "New Directions for Low-Dimensional Thermoelectric Materials," *Advanced Materials,* vol. 19, pp. 1043-1053, 2007.

[11] G. Chen, *Nanoscale Energy Transport and Conversion*. New York, New York: Oxford University Press, 2005.

[12] A. I. Hochbaum, R. Chen, R. D. Delgado, W. Liang, E. C. Garnett, M. Najarian, A. Majumdar, and P. Yang, "Enhanced thermoelectric performance of rough silicon nanowires," *Nature,* vol. 451, pp. 163-167, 2008.

[13] D. Kraemer, B. Poudel, H.-P. Feng, J. C. Caylor, B. Yu, X. Yan, Y. Ma, X. Wang, D. Wang, A. Muto, K. McEnaney, M. Chiesa, Z. Ren, and G. Chen, "High-performance flat-panel solar thermoelectric generators with high thermal concentration," *Nature Materials,* vol. 10, 2011.

[14]   H. Bottner, G. Chen, and R. Venkatasubramanian, "Aspects of Thin-Film Superlattice Thermoelectric Materials, Devices, and Applications," *MRS Bulletin,* vol. 31, pp. 211-217, March 2006.

[15]   C. J. Vineis, A. Shakouri, A. Majumdar, and M. G. Kanatzidis, "Nanostructured Thermoelectrics: Big Efficiency Gains from Small Features," *Advanced Materials,* vol. 22, pp. 3970-3980, 2010.

[16]   J. P. Fleurial, T. Caillat, B. J. Nesmith, R. C. Ewell, D. F. Woerner, G. C. Carr, and L. E. Jones, "Thermoelectrics: From Space Power Systems to Terrestrial Waste Heat Recovery Applications," in *2nd Thermoelectrics Applications Workshop*, San Diego, California, 2011.

[17]   Available: voyager.jpl.nasa.gove/spacecraft/instruments_rtg.html

[18]   *Marlow Industries, Inc.* Available: www.marlow.com

[19]   *Perpetua.* Available: www.perpetuapower.com

[20]   *National Science Foundation Innovation Corps (I-Corps).* Available: www.nsf.gov/news/special_reports/i-corps/

[21]   G. S. Nolas, J. Poon, and M. Kanatzidis, "Recent developments in buk thermoelectric materials," *MRS Bulletin,* vol. 31, 2006.

[22]   G. G. Yadav, J. A. Susoreny, G. Zhang, H. Yang, and Y. Wu, "Nanostructure-based thermoelectric conversion: an insight into the feasibility and sustainability for large-scale deployment," *Nanoscale,* vol. 3, pp. 3555-3562, 2011.

[23]   D. T. Crane, "Thermoelectric Generator Performance for Passenger Vehicles," presented at the 3rd Thermoelectrics Applications Workshop, Baltimore, MD, 2012.

[24]   L. Aixala, "RENOTER Project," in *3rd Thermoelectrics Applications Workshop*, Baltimore, MD, 2012.

[25]   D. T. Crane and D. Kossakovski, "High Heat Flux Thermoelectric Module Using Standard Bulk Material," in *3rd Thermoelectrics Applications Workshop*, Baltimore, MD, 2012.

[26]   G. Meisner, "Skutterudite Thermoelectric Generator for Automotive Waste Heat Recovery," in *3rd Thermoelectrics Applications Workshop*, Baltimore, MD, 2012.

[27]   *Alphabet Energy*. Available: www.alphabetenergy.com

[28]   *GMZ Energy*. Available: www.gmzenergy.com

[29]   *Phononic Devices*. Available: www.phononicdevices.com

[30]   *Sheetak*. Available: www.sheetak.com

[31]   K. Yazawa and A. Shakouri, "Cost-efficiency trade-off and the design of thermoelectric power generators," *Environ Sci Technol,* vol. 45, pp. 7548-53, Sep 1 2011.

[32]   C. Wadia, P. Albertus, and V. Srinivasan, "Resource constraints on the battery energy storage potential for grid and transportation applications," *Journal of Power Sources,* vol. 196, pp. 1593-1598, 2011.

[33]   C. Wadia, A. P. Alivisatos, and D. M. Kammen, "Materials Availability Expands the Opportunity for Large-Scale Photovoltaics Deployment," *Environ Sci Technol,* vol. 43, pp. 2072-2077, 2009/03/15 2009.

[34]   S. W. Angrist, *Direct Energy Conversion*. Boston: Allyn and Bacon, Inc., 1965.

[35]   G. Min and D. M. Rowe, "Conversion efficiency of thermoelectric combustion systems," *IEEE Transactions on Energy Conversion,* vol. 22, 2007.

[36]   M. D. Rowe, G. Min, S. G. K. Williams, A. Aoune, K. Matsuura, V. L. Kuznetsov, and L. W. Fu, "Thermoelectric recoversy of waste heat - case studies," in *32nd Intersociety Energy Conversion Engineering Conference*, 1997.

[37]   G. Snyder and T. Ursell, "Thermoelectric Efficiency and Compatibility," *Physical Review Letters,* vol. 91, 2003.

[38]   R. K. Shah, Sekuli, and D. a. P., "Fundamentals of Heat Exchanger Design," ed: John Wiley & Sons.

[39]   F. P. Incropera, D. P. Dewitt, T. L. Bergman, and A. S. Lavine, *Fundamentals of Heat and Mass Transfer*, 6th ed.: John Wiley & Sons, 2007.

[40]   T. Hendricks and W. T. Choate, "Engineering Scoping Study of Thermoelectric Generator Systems for Industrial Waste Heat Recovery," US Dept. of Energy-Industrial Technologies Program2006.

[41]   McMaster-Carr, "McMaster-Carr," ed.

[42]   L. M. Matthews, *Estimating Manufacturing Costs: A Practical Guide for Managers and Estimators*. New York: McGraw-Hill, 1983.

[43] U. S. G. Survey. *Commodity Statistics and Information*. Available: http://minerals.usgs.gov/minerals/pubs/commodity/

[44] "<Installed solar PV system prices.pdf>."

[45] A. Miner, "The Industrialization of Thermoelectric Power Generation Technology," in *3rd Thermoelectrics Applications Workshop*, Baltimore, MD, 2012.

[46] Tom Carver Science & Engineering Associate, "Science & Engineering Associate, Flexible Cleanroom and Microfab Shop, Stanford Nano Center," ed, 2012.

[47] *Praxair*. Available: www.praxair.com/semiconductor

[48] *Sigma-Aldrich*. Available: www.sigmaaldrich.com

[49] *Kurt J. Lesker Company*. Available: www.lesker.com

[50] U.S. Geological Survey: Commodity Statistics and Information, "U.S. Geological Survey: Commodity Statistics and Information," U. S. D. o. t. Interior, Ed., ed, 2011.

[51] M. Beekman and G. S. Nolas, "Inorganic clathrate-II materials of group 14: synthetic routes and physical properties," *Journal of Materials Chemistry,* vol. 18, p. 842, 2008.

[52] A. D. LaLonde, Y. Pei, H. Wang, and G. Jeffrey Snyder, "Lead telluride alloy thermoelectrics," *Materials Today,* vol. 14, pp. 526-532, 2011.

[53] N. D. Lowhorn, W. Wong-Ng, Z.-Q. Lu, J. Martin, M. L. Green, J. E. Bonevich, E. L. Thomas, N. R. Dilley, and J. Sharp, "Development of a Seebeck coefficient Standard Reference Material™," *Journal of Materials Research,* vol. 26, pp. 1983-1992, 2011.

[54] *Fritsch GmbH*. Available: www.fritsch-milling.com

[55] *Buehler*. Available: www.buehler.com

[56] *Thermal Technology LLC*. Available: thermaltechnology.com

[57] *Disco*. Available: www.disco.co.jp

[58] *Bid-Service LLC*. Available: www.bidservice.com

[59]   Sylvain Muckenhirn VP of Process & Manufacturing at Alphabet Energy, "Sylvain Muckenhirn, VP of Process & Manufacturing, Alphabet Energy," ed, 2012.

[60]   Taiwan Semiconductor Manufacturing Company, "Taiwan Semiconductor Manufacturing Company," ed, 2012.

[61]   Tse Ng Xerox PARC, "Tse Ng, Xerox PARC," ed, 2012.

[62]   *Dimatix Materials Printer*. Available: www.fujifilmusa.com

[63]   T. J. Hendricks, "Micro- and Nano-Technologies Enabling More Compact, Lightweight Thermoelectric Power Generation and Cooling Systems," in *3rd Thermoelectrics Applications Workshop*, Baltimore, MD, 2012.

[64]   M. Scholdt, H. Do, J. Lang, A. Gall, A. Colsmann, U. Lemmer, J. Koenig, M. Winkler, and H. Boettner, "Organic Semiconductors for Thermoelectric Applications," *Journal of Electronic Materials,* vol. 39, pp. 1589-1592.

[65]   W. J. Parker and R. J. Jenkins, "THERMAL CONDUCTIVITY MEASUREMENTS ON BISMUTH TELLURIDE IN THE PRESENCE OF A 2 MEV ELECTRON BEAM," USNRDL-TR-462 Country unknown/Code not availableTue Feb 05 15:47:45 EST 2008DTIE; NSA-15-004387English, 1960.

[66]   W. Xie, X. Tang, Y. Yan, Q. Zhang, and T. M. Tritt, "High thermoelectric performance BiSbTe alloy with unique low-dimensional structure," *Journal of Applied Physics,* vol. 105, p. 113713, 2009.

[67]   J. Zhou, C. Jin, J. H. Seol, X. Li, and L. Shi, "Thermoelectric properties of individual electrodeposited bismuth telluride nanowires," *Applied Physics Letters,* vol. 87, p. 133109, 2005.

[68]   Y. Pei, N. A. Heinz, A. LaLonde, and G. J. Snyder, "Combination of large nanostructures and complex band structure for high performance thermoelectric lead telluride," *Energy & Environmental Science,* vol. 4, p. 3640, 2011.

[69]   T. C. Harman, P. J. Taylor, M. P. Walsh, and B. E. LaForge, "Quantum dot superlattice thermoelectric materials and devices," *Science,* vol. 297, pp. 2229-32, Sep 27 2002.

[70]   K. F. Hsu, S. Loo, F. Guo, W. Chen, J. S. Dyck, C. Uher, T. Hogan, E. K. Polychroniadis, and M. G. Kanatzidis, "Cubic AgPbmSbTe2+m: Bulk

Thermoelectric Materials with High Figure of Merit," *Science,* vol. 303, pp. 818-821, February 6, 2004 2004.

[71] G. Joshi, H. Lee, Y. Lan, X. Wang, G. Zhu, D. Wang, R. W. Gould, D. C. Cuff, M. Y. Tang, M. S. Dresselhaus, G. Chen, and Z. Ren, "Enhanced Thermoelectric Figure-of-Merit in Nanostructured p-type Silicon Germanium Bulk Alloys," *NanoLetters,* vol. 8, pp. 4670-4674, 2008.

[72] J. A. Martinez, P. P. Provencio, S. T. Picraux, J. P. Sullivan, and B. S. Swartzentruber, "Enhanced thermoelectric figure of merit in SiGe alloy nanowires by boundary and hole-phonon scattering," *Journal of Applied Physics,* vol. 110, p. 074317, 2011.

[73] S. K. Bux, M. T. Yeung, E. S. Toberer, G. J. Snyder, R. B. Kaner, and J.-P. Fleurial, "Mechanochemical synthesis and thermoelectric properties of high quality magnesium silicide," *Journal of Materials Chemistry,* vol. 21, p. 12259, 2011.

[74] V. K. Zaitsev, M. I. Fedorov, E. A. Gurieva, I. S. Eremin, P. P. Konstantinov, A. Y. Samunin, and M. V. Vedernikov, "Highly effective Mg_{2}Si_{1−x}Sn_{x} thermoelectrics," *Physical Review B,* vol. 74, p. 045207, 2006.

[75] S. K. Bux, R. G. Blair, P. K. Gogna, H. Lee, G. Chen, M. S. Dresselhaus, R. B. Kaner, and J.-P. Fleurial, "Nanostructured Bulk Silicon as an Effective Thermoelectric Material," *Advanced Functional Materials,* vol. 19, pp. 2445-2452, 2009.

[76] A. I. Hochbaum, R. Chen, R. D. Delgado, W. Liang, E. C. Garnett, M. Najarian, A. Majumdar, and P. Yang, "Enhanced thermoelectric performance of rough silicon nanowires," *Nature,* vol. 451, pp. 163-7, Jan 10 2008.

[77] X. Chen, A. Weathers, A. Moore, J. Zhou, and L. Shi, "Thermoelectric Properties of Cold-Pressed Higher Manganese Silicides for Waste Heat Recovery," *Journal of Electronic Materials,* vol. 41, pp. 1564-1572, 2012.

[78] D. Cederkrantz, M. Nygren, and A. E. C. Palmqvist, "Thermoelectric properties of partly Sb- and Zn-substituted Ba[sub 8]Ga[sub 16]Ge[sub 30] clathrates," *Journal of Applied Physics,* vol. 108, p. 113711, 2010.

[79] E. Toberer, M. Christensen, B. Iversen, and G. Snyder, "High temperature thermoelectric efficiency in Ba8Ga16Ge30," *Physical Review B,* vol. 77, 2008.

[80] J. H. Roudebush, E. S. Toberer, H. Hope, G. Jeffrey Snyder, and S. M. Kauzlarich, "Crystal structure, characterization and thermoelectric properties of the type-I clathrate Ba8−ySryAl14Si32 (0.6≤y≤1.3) prepared by aluminum flux," *Journal of Solid State Chemistry,* vol. 184, pp. 1176-1185, 2011.

[81] P. F. Qiu, J. Yang, R. H. Liu, X. Shi, X. Y. Huang, G. J. Snyder, W. Zhang, and L. D. Chen, "High-temperature electrical and thermal transport properties of fully filled skutterudites RFe4Sb12 (R = Ca, Sr, Ba, La, Ce, Pr, Nd, Eu, and Yb)," *Journal of Applied Physics,* vol. 109, p. 063713, 2011.

[82] J. Peng, J. He, P. N. Alboni, and T. M. Tritt, "Synthesis and Thermoelectric Properties of the Double-Filled Skutterudite Yb0.2In y Co4Sb12," *Journal of Electronic Materials,* vol. 38, pp. 981-984, 2009.

[83] M. Puyet, A. Dauscher, B. Lenoir, M. Dehmas, C. Stiewe, E. Muller, and J. Hejtmanek, "Beneficial effect of Ni substitution on the thermoelectric properties in partially filled Ca[sub y]Co[sub 4 - x]Ni[sub x]Sb[sub 12] skutterudites," *Journal of Applied Physics,* vol. 97, p. 083712, 2005.

[84] J. P. Heremans, V. Jovovic, E. S. Toberer, A. Saramat, K. Kurosaki, A. Charoenphakdee, S. Yamanaka, and G. J. Snyder, "Enhancement of thermoelectric efficiency in PbTe by distortion of the electronic density of states," *Science,* vol. 321, pp. 554-7, Jul 25 2008.

[85] G. Xu, R. Funahashi, M. Shikano, I. Matsubara, and Y. Zhou, "Thermoelectric properties of the Bi- and Na-substituted Ca[sub 3]Co[sub 4]O[sub 9] system," *Applied Physics Letters,* vol. 80, p. 3760, 2002.

[86] S. C. Andrews, M. A. Fardy, M. C. Moore, S. Aloni, M. Zhang, V. Radmilovic, and P. Yang, "Atomic-level control of the thermoelectric properties in polytypoid nanowires," *Chemical Science,* vol. 2, p. 706, 2011.

[87] K. Fujita, T. Mochida, and K. Nakamura, "High-temperature thermoelectric properties of NaxCoO2 single crystals," in *International Conference on Thermoelectrics*, 2001, pp. 168-171.

[88] S. Sakurada and N. Shutoh, "Effect of Ti substitution on the thermoelectric properties of (Zr,Hf)NiSn half-Heusler compounds," *Applied Physics Letters,* vol. 86, p. 082105, 2005.

[89] Q. Shen, L. Chen, T. Goto, T. Hirai, J. Yang, G. P. Meisner, and C. Uher, "Effects of partial substitution of Ni by Pd on the thermoelectric properties of ZrNiSn-based half-Heusler compounds," *Applied Physics Letters,* vol. 79, p. 4165, 2001.

[90] T. Katayama, S. Kim, Y. Kimura, and Y. Mishima, "The effects of quaternary additions on thermoelectric properties of TiNiSn-based half-heusler alloys," *Journal of Electronic Materials,* vol. 32, pp. 1160-1165, 2003.

[91] P. F. Qiu, J. Yang, R. H. Liu, X. Shi, and X. Y. Huang, "High-temperature electrical and thermal transport properties of fully filled skutterudites RFe4Sb12 (R = Ca, Sr, Ba, La, Ce, Pr, Nd, Eu, and Yb)," *Journal of Applied Physics,* vol. 109, 2011.

[92] R. Venkatasubramanian, E. Siivola, T. Colpitts, and B. O'Quinn, "Thin-film thermoelectric devices with high room-temperature figures of merit," *Nature,* vol. 413, pp. 597-602, October 11, 2001 2001.

[93] D. M. Powell, M. T. Winkler, H. J. Choi, C. B. Simmons, D. B. Needleman, and T. Buonassisi, "Crystalline silicon photovoltaics: a cost analysis framework for determining technology pathways to reach baseload electricity costs," *Energy & Environmental Science,* vol. 5, p. 5874, 2012.

[94] F. Vélez, J. J. Segovia, M. C. Martín, G. Antolín, F. Chejne, and A. Quijano, "A technical, economical and market review of organic Rankine cycles for the conversion of low-grade heat for power generation," *Renewable and Sustainable Energy Reviews,* vol. 16, pp. 4175-4189, 2012.

[95] F. E. R. Commission, "The potential benefits of distributed generation and rate-related issues that may impede their expansion," U. S. D. o. Energy, Ed., ed, 2007.

[96] J. W. LaGrandeur, L. E. Bell, and D. T. Crane, "Recent Progress in Thermoelectric Power Generation Systems for Commercial Applications," in *Materials Research Society Symposium*, 2011.

[97]   S. LeBlanc, Y. Gao, and K. E. Goodson, "Thermoelectric Heat Recovery from a Tankless Water Heating System," in *2008 ASME International Mechanical Engineering Congress and Exposition*, Boston, Massachusetts, 2008.

[98]   D. T. Crane and G. S. Jackson, "Optimization of cross flow heat exchangers for thermoelectric waste heat recovery," *Energy Conversion and Management,* vol. 45, pp. 1565-1582, 2004.

[99]   X. Niu, J. Yu, and S. Wang, "Experimental study on low-temperature waste heat thermoelectric generator," *Journal of Power Sources,* vol. 188, pp. 621-626, 2009.

[100]   M. A. Karri, E. F. Thacher, and B. T. Helenbrook, "Exhaust energy conversion by thermoelectric generator: Two case studies," *Energy Conversion and Management,* vol. 52, pp. 1596-1611, 2011.

[101]   A. M. Pettes, M. S. Hodes, and K. E. Goodson, "Optimized thermoelectric refrigeration in the presence of thermal boundary resistance," *IEEE Transactions on Advanced Packaging,* vol. 32, 2009.

[102]   T. Tong, Y. Zhao, L. Delzeit, A. Kashani, M. Meyyappan, and A. Majumdar, "Dense vertically aligned multiwalled carbon nanotube arrays as thermal interface materials," *IEEE Transactions on Components and Packaging Technologies,* vol. 30, 2007.

[103]   M. A. Panzer, G. Zhang, D. Mann, X. Hu, E. Pop, H. Dai, and K. E. Goodson, "Thermal Properties of Metal-Coated Vertically Aligned Single-Wall Nanotube Arrays," *Journal of Heat Transfer,* vol. 130, p. 052401, 2008.

[104]   Y. Won, Y. Gao, M. A. Panzer, S. Dogbe, L. Pan, T. W. Kenny, and K. E. Goodson, "Mechanical characterization of aligned multi-walled carbon nanotube films using microfabricated resonators," *Carbon,* vol. 50, pp. 347-355, 2012.

[105]   Y. Gao, A. M. Marconnet, M. A. Panzer, S. LeBlanc, S. Dogbe, Y. Ezzahri, A. Shakouri, and K. E. Goodson, "Nanostructured Interfaces for Thermoelectrics," *Journal of Electronic Materials,* vol. 39, pp. 1456-1462, 2010.

[106]   Y. Gao, T. Kodama, Y. Won, S. Dogbe, L. Pan, and K. E. Goodson, "Impact of nanotube density and alignment on the elastic modulus near the top and base surfaces of aligned multi-walled carbon nanotube films," *Carbon,* 2012.

[107] J. Fairbanks, "Vehicular Thermoelectrics: A New Green Technology," in *2011 Thermoelectrics Applications Workshop*, D. o. Energy, Ed., ed. San Diego, CA, 2011.

[108] T. J. Hendricks and W. T. Choate, "Engineering scoping study of thermoelectric generator systems for industrial waste heat recovery," D. o. Energy, Ed., ed, 2006.

[109] M. Chen, S.-S. Lu, and B. Liao, "On the Figure of Merit of Thermoelectric Generators," *Journal of Energy Resources Technology,* vol. 127, p. 37, 2005.

[110] J. Esarte, G. Min, and D. M. Rowe, "Modelling heat exchangers for thermoelectric generators," *Journal of Power Sources,* vol. 93, 2001.

[111] T. J. Hendricks, "Thermal System Interactions in Optimizing Advanced Thermoelectric Energy Recovery Systems," *Journal of Energy Resources Technology,* vol. 129, p. 223, 2007.

[112] R. B. Peterson, "The Maximum Power Operating Point for a Combustion-Driven Thermoelectric Converter With Heat Recirculation," *Journal of Engineering for Gas Turbines and Power,* vol. 129, p. 1106, 2007.

[113] F. P. Incropera, D. P. Dewitt, T. L. Bergman, and A. S. Lavine, *Fundamentals of Mass and Heat Transfer*. New York: McGraw-Hill, 2007.

[114] J. B. Heywood, *Internal Combustion Engine Fundamentals*. USA: McGraw-Hill, Inc., 1988.

[115] R. Stone, *Introduction to Internal Combustion Engines*, Third edition ed. Warrendale, Pa: Society of Automotive Engineers, Inc., 1999.

[116] S. LeBlanc, S. K. Yee, M. Scullin, C. Dames, and K. E. Goodson, "Title," unpublished|.

[117] M. A. McNeil and N. Bojda, "Cost-effectiveness of high-efficiency appliances in the U.S. residential sector: A case study," *Energy Policy,* 2012.

[118] T. J. Hendricks and J. A. Lustbader, "Advanced thermoelectric power system investigations for light-duty and heavy-duty applications: Part I," presented at the 21st International Conference on Thermoelectrics, 2002.

[119] T. J. Hendricks and J. A. Lustbader, "Advanced thermoelectric power system investigations for light-duty and heavy-duty applications: Part II," presented at the 21st International Conference on Thermoelectrics, 2002.

[120] Bosch. Available: http://www.boschhotwater.com/

[121] N. Kloub, "Improving the gas instantaneous water heaters performanc," *American Journal of Applied Sciences,* vol. 2, 2005.

[122] G. Min and D. M. Rowe, "Ring-structured thermoelectric module," *Semiconductor Science and Technology,* vol. 22, pp. 880-883, 2007.

[123] W. M. Kays and A. L. London, *Compact Heat Exchangers*. New York: McGraw-Hill, 1984.

[124] *CRC Handbook of Thermoelectrics*. Boca Raton: CRC Press, 1995.

[125] R. Prasher, "Thermal Interface Materials: Historical Perspective, Status, and Future Directions," *Proceedings of the IEEE,* vol. 94.

[126] P. M. Mayer and R. J. Ram, "Optimization of Heat Sink–Limited Thermoelectric Generators," *Nanoscale and Microscale Thermophysical Engineering,* vol. 10, pp. 143-155, 2006.

[127] K. E. Goodson, "Automotive Thermoelectric Modules with Scalable Thermo- and Electro-Mechanical Interfaces," in *2011 Thermoelectrics Applications Workshop*, San Diego, CA, 2011.

[128] J.-P. Colinge, C.-W. Lee, A. Afzalian, N. D. Akhavan, R. Yan, I. Ferain, P. Razavi, B. O'Neil, A. Blake, M. White, A.-M. Kelleher, B. McCarthy, and R. Murphy, "Nanowire transistors without junctions," *Nature nanotechnology,* vol. 5, 2010.

[129] J. Goldberger, D. J. Sirbuly, M. Law, and P. Yang, "ZnO Nanowire Transistors," *Society,* pp. 9-14, 2005.

[130] F. Patolsky and C. M. Lieber, "Nanowire nanosensors," *Materials Today,* 2005.

[131] A. Menzel, K. Subannajui, F. Guder, D. Moser, O. Paul, and M. Zacharias, "Multifunctional ZnO-Nanowire-Based Sensor," *Advanced Functional Materials,* vol. 21, pp. 4342-4348, 2011.

[132] A. I. Hochbaum and P. Yang, "Semiconductor Nanowires for Energy Conversion," *Chemical Reviews,* vol. 110, pp. 527-546, 2010.

[133] S. C. Andrews, M. A. Fardy, M. C. Moore, S. Aloni, M. Zhang, V. Radmilovic, and P. Yang, "Atomic-level control of the thermoelectric properties in polytypoind nanowires," *Chemical Science,* vol. 2, pp. 706-714, 2011.

[134] J. A. Martinez, P. P. Provencio, S. T. Picraux, J. P. Sullivan, and B. S. Swartzentruber, "Enhanced thermoelectric figure of merit in SiGe alloy nanowires by boundary and hole-phonon scattering," *Journal of Applied Physics,* vol. 110, 2011.

[135] E. C. Garnett, M. L. Brongersma, Y. Cui, and M. D. McGehee, "Nanowire Solar Cells," *Annual Review of Materials Research,* vol. 41, 2011.

[136] C. K. Chan, R. N. Patel, M. J. O'Connell, B. A. Korgel, and Y. Cui, "Solution-Grown Silicon Nanowires for Lithium-Ion Battery Anodes," *ACS Nano,* vol. 4, pp. 1443-1450, 2010.

[137] S. R. Gowda, A. L. M. Reddy, X. Zhan, and P. M. Ajayan, "Building Energy Storage Device on a Single Nanowire," *Nano letters,* vol. 11, pp. 3329-3333, 2011.

[138] C. K. Chan, H. Peng, G. Liu, K. McIlwrath, X. F. Zhang, R. A. Huggins, and Y. Cui, "High-performance lithium battery anodes using silicon nanowires," *Nature nanotechnology,* vol. 3, 2008.

[139] U. Ozgur, Y. I. Alivov, A. Teke, M. A. Reshchikov, S. Dogan, V. Avrutin, S.-J. Cho, and H. Morkoc, "A comprehensive review of ZnO materials and devices," *Journal of Applied Physics,* vol. 98, 2005.

[140] A. B. Djurisic, X. Chen, Y. H. Leung, and A. M. C. Ng, "ZnO nanostructures: growth, properties and applications," *Journal of Materials Chemistry,* 2012.

[141] P. Jood, R. J. Mehta, Y. Zhang, G. Peleckis, X. Wang, R. W. Siegel, T. Borca-Tasciuc, S. X. Dou, and G. Ramanath, "Al-Doped Zinc Oxide Nanocomposites with Enhanced Thermoelectric Properties," *NanoLetters,* vol. 11, pp. 4337-4342, 2011.

[142] L. J. Brillson and Y. Lu, "ZnO Schottky barriers and Ohmic contacts," *Journal of Applied Physics,* vol. 109, 2011.

[143] Z. Zhang, K. Yao, Y. Liu, C. Jin, X. Liang, Q. Chen, and L.-M. Peng, "Quantitative Analysis of Current-Voltage Characteristics of Semiconducting Nanowires: Decoupling of Contact Effects," *Advanced Functional Materials,* vol. 17, pp. 2478-2489, 2007.

[144] Y.-F. Lin and W.-B. Jian, "The Impact of Nanocontact on Nanowire Based Nanoelectronics," *NanoLetters,* vol. 8, pp. 3146-3150, 2008.

[145] R. Prasher, "Acoustic mismatch model for thermal contact resistance of van der Waals contacts," *Applied Physics Letters,* vol. 94, p. 041905, 2009.

[146] F. Zhou, A. Persson, L. Samuelson, H. Linke, and L. Shi, "Thermal resistance of a nanoscale point contact to an indium arsenide nanowire," *Applied Physics Letters,* vol. 99, 2011.

[147] T. Westover, R. Jones, J. Y. Huang, G. Wang, E. Lai, and A. A. Talin, "Photoluminescence, Thermal Transport, and Breakdown in Joule-Heated GaN Nanowires," *NanoLetters,* vol. 9, pp. 257-263, 2009.

[148] A. Liao, R. Alizadegan, Z.-Y. Ong, S. Dutta, F. Xiong, K. J. Hsia, and E. Pop, "Thermal dissipation and variability in electrical breakdown of carbon nanotube devices," *Physical Review B,* vol. 82, 2010.

[149] K. Nagashima, T. Yanagida, A. Klamchuen, M. Kanai, K. Oka, S. Seki, and T. Kawai, "Interfacial effect on metal/oxide nanowire junctions," *Applied Physics Letters,* vol. 96, 2010.

[150] L. Goris, R. Noriega, M. Donovan, J. Jokisaari, G. Kusinski, and A. Salleo, "Intrinsic and Doped Zinc Oxide Nanowires for Transparent Electrode Fabrication via Low-Temperature Solution Synthesis," *Journal of Electronic Materials,* vol. 38, pp. 586-595, April 2009 2009.

[151] S. M. Sze and K. K. Ng, *Physics of Semiconductor Devices*, 3 ed. Hoboken, NJ: Wiley-Interscience, 2007.

[152] E. Schlenker, A. Bakin, T. Weimann, P. Hinze, D. H. Weber, A. Golzhauser, H.-H. Wehmann, and A. Waag, "On the difficulties in characterizing ZnO nanowires," *Nanotechnology,* vol. 19, 2008.

[153] V. Bahadur, J. Xu, Y. Liu, and T. S. Fisher, "Thermal Resistance of Nanowire-Plane Interfaces," *Journal of Heat Transfer,* vol. 127, p. 664, 2005.

[154] R. Prasher, "Predicting the Thermal Resistance of Nanosized Constrictions," *NanoLetters,* vol. 5, pp. 2155-2159, 2005.

[155] C. Yu, S. Saha, J. Zhou, L. Shi, A. M. Cassell, B. A. Cruden, Q. Ngo, and J. Li, "Thermal Contact Resistance and Thermal Conductivity of a Carbon Nanofiber," *Journal of Heat Transfer,* vol. 128, 2006.

[156] E. Pop, D. A. Mann, K. E. Goodson, and H. Dai, "Electrical and thermal transport in metallic single-wall carbon nanotubes on insulating substrates," *Journal of Applied Physics,* vol. 101, 2007.

[157] J. Niemann. (2005, Electrical Measurements on Nanoscale Materials.

[158] J. Appenzeller, M. Radosavljević, J. Knoch, and P. Avouris, "Tunneling Versus Thermionic Emission in One-Dimensional Semiconductors," *Physical Review Letters,* vol. 92, p. 048301, 2004.

[159] E. H. Rhoderick, *Metal-semiconductor contacts*, 2nd ed. ed. Oxford [England] :: Claredon Press ;, 1988.

[160] F. A. Padovani and R. Stratton, "Field and thermionic-field emission in Schottky barriers," *Solid-State Electronics,* vol. 9, pp. 695-707, 1966.

[161] C. Y. Chang and S. M. Sze, "Carrier transport across metal-semiconductor barriers," *Solid-State Electronics,* vol. 13, pp. 727-740, 1970.

[162] S. E. Mohney, Y. Wang, M. A. Cabassi, K. K. Lew, S. Dey, J. M. Redwing, and T. S. Mayer, "Measuring the specific contact resistance of contacts to semiconductor nanowires," *Solid-State Electronics,* vol. 49, pp. 227-232, 2005.

[163] H. H. Berger, "Models for contacts to planar devices," *Solid-State Electronics,* vol. 15, pp. 145-158, 1972.

[164] L. M. Mansfield, K. a. Bertness, P. T. Blanchard, T. E. Harvey, a. W. Sanders, and N. a. Sanford, "GaN Nanowire Carrier Concentration Calculated from Light and Dark Resistance Measurements," *Journal of Electronic Materials,* vol. 38, pp. 495-504, 2009.

[165] B. S. Simpkins, M. A. Mastro, C. R. Eddy, and P. E. Pehrsson, "Surface depletion effects in semiconducting nanowires," *Journal of Applied Physics,* vol. 103, 2008.

[166] S. A. Phadke, Y. Park, F. B. Prinz, and A. Salleo, "A study of the cause of high nanowire to nanowire junction resistance in conducting ZnO nanowire mats," 2012.

[167] K. L. Grosse, M.-H. Bae, F. Lian, E. Pop, and W. P. King, "Nanoscale Joule heating, Peltier cooling and current crowding at graphene-metal contacts," *Nature Nanotechnology,* vol. 6, 2011.

[168] H. Fritzsche, "A general expression for the thermoelectric power," *Solid State Communications,* vol. 9, pp. 1813-1815, 1971.

[169] E. Schlenker, A. Bakin, T. Weimann, P. Hinze, D. H. Weber, A. Golzhauser, H. H. Wehmann, and A. Waag, "On the difficulties in characterizing ZnO nanowires," *Nanotechnology,* vol. 19, p. 365707, Sep 10 2008.

[170] I. Park, Z. Li, A. P. Pisano, and R. S. Williams, "Top-down fabricated silicon nanowire sensors for real-time chemical detection.," *Nanotechnology,* vol. 21, p. 015501, 2010.

[171] M. T. Björk, H. Schmid, J. Knoch, H. Riel, and W. Riess, "Donor deactivation in silicon nanostructures.," *Nature nanotechnology,* vol. 4, pp. 103-7, 2009.

[172] H. D. Tong, S. Chen, W. G. van der Wiel, E. T. Carlen, and A. van den Berg, "Novel top-down wafer-scale fabrication of single crystal silicon nanowires.," *Nano letters,* vol. 9, pp. 1015-22, 2009.

[173] K.-K. Lew, L. Pan, T. E. Bogart, S. M. Dilts, E. C. Dickey, J. M. Redwing, Y. Wang, M. Cabassi, T. S. Mayer, and S. W. Novak, "Structural and electrical properties of trimethylboron-doped silicon nanowires," *Applied Physics Letters,* vol. 85, p. 3101, 2004.

[174] S. Habicht, Q. T. Zhao, S. F. Feste, L. Knoll, S. Trellenkamp, B. Ghyselen, and S. Mantl, "Electrical characterization of strained and unstrained silicon nanowires with nickel silicide contacts.," *Nanotechnology,* vol. 21, p. 105701, 2010.

[175] E. Stern, G. Cheng, M. P. Young, and M. a. Reed, "Specific contact resistivity of nanowire devices," *Applied Physics Letters,* vol. 88, p. 053106, 2006.

[176] A. Motayed, A. V. Davydov, S. N. Mohammad, and J. Melngailis, "Experimental investigation of electron transport properties of gallium nitride nanowires," *Journal of Applied Physics,* vol. 104, p. 024302, 2008.

[177] G. Ye, K. Shi, R. Burke, J. M. Redwing, and S. E. Mohney, "Ti/Al Ohmic Contacts to n-Type GaN Nanowires," *Journal of Nanomaterials,* vol. 2011, 2011.

[178] C. Hwang, J.-H. Hyung, S.-Y. Lee, C.-O. Jang, T.-H. Kim, P. Choi, and S.-K. Lee, "The formation and characterization of electrical contacts (Schottky and Ohmic) on gallium nitride nanowires," *Journal of Physics D: Applied Physics,* vol. 41, pp. 159802-159802, 2008.

[179] T. Weimann, P. Hinze, E. Schlenker, a. Bakin, a. C. Mofor, a. Behrends, and a. Waag, "Electrical and structural characterisation of single ZnO nanorods," *Microelectronic Engineering,* vol. 85, pp. 1248-1252, 2008.

[180] J. H. He, P. H. Chang, C. Y. Chen, and K. T. Tsai, "Electrical and optoelectronic characterization of a ZnO nanowire contacted by focused-ion-beam-deposited Pt.," *Nanotechnology,* vol. 20, p. 135701, 2009.

[181] G.-D. Yuan, W.-J. Zhang, J.-S. Jie, X. Fan, J.-X. Tang, I. Shafiq, Z.-Z. Ye, C.-S. Lee, and S.-T. Lee, "Tunable n-Type Conductivity and Transport Properties of Ga-doped ZnO Nanowire Arrays," *Advanced Materials,* vol. 20, pp. 168-173, 2008.